Monitoring a Mechanochemical Reaction Reveals the Formation of a New ACC Defect Variant Containing the HCO 3 – Anion Encapsulated by an Amorphous Matrix

Phil Opitz, Maria Asta, Alejandro Fernandez-Martinez, Martin Panthöfer, Anke Kabelitz, Franziska Emmerling, Mihail Mondeshki, Wolfgang Tremel

Monitoring a Mechanochemical Reaction Reveals the Formation of Stable Alkaline Earth (Ca, Sr, Ba) Hydrogen Carbonates Encapsulated by an Amorphous Phase

Phil Opitz,[a] Maria P. Asta,[b] Alejandro Fernandez-Martinez,[b] Martin Panthöfer,[a] Anke Kabelitz,[c] Franziska Emmerling,[c,d] Mihail Mondeshki,[a]* and Wolfgang Tremel[a]*

[a] Institut für Anorganische Chemie und Analytische Chemie, Johannes Gutenberg-Universität Mainz, Duesbergweg 10-14, D-55128 Mainz, Germany
[b] Univ. Grenoble Alpes, Univ. Savoie Mont Blanc, CNRS, IRD, IFSTTAR, ISTerre, 38000 Grenoble, France
[c] Bundesanstalt für Materialforschung und -prüfung (BAM), Richard-Willstätter-Straße 11, D–12489 Berlin, Germany
[d] Institut für Chemie, Humboldt-Universität zu Berlin, Brook-Taylor-Straße 2, D-12489 Berlin, Germany

ABSTRACT

Amorphous calcium carbonate (ACC) is an important precursor in the biomineralization of crystalline $CaCO_3$. In nature it serves as a storage material or as permanent structural element, whose lifetime is regulated by an organic matrix. The relevance of ACC in materials science is primarily related to our understanding of $CaCO_3$ crystallization pathways and $CaCO_3$/(bio)polymer nanocomposites. ACC can be synthesized by liquid-liquid phase separation, and it is typically stabilized with macromolecules. We have prepared ACC by milling calcite in a planetary ball mill. Ball-milled amorphous calcium carbonate (BM-ACC) was stabilized with monetite ($CaHPO_4$). The addition of phosphate ions from $CaHPO_4$ generates a strained network that hinders recrystallization kinetically. In comparison to wet-chemically prepared ACC, ball-milling forms anhydrous BM-ACC. The amorphization process and the structure of BM-ACC were studied by quantitative Fourier transform infrared spectroscopy and solid state ^{31}P, ^{13}C, and ^{1}H magic angle spinning nuclear magnetic resonance spectroscopy, which are highly sensitive to symmetry changes of the local environment. In the first - and fast - reaction step, the CO_3^{2-} anions are protonated by the HPO_4^{2-} groups. The formation of unprecedented hydrogen carbonate (HCO_3^-) and orthophosphate anions appears to be the driving force of the reaction, because the phosphate group has a higher Coulomb energy and the

tetrahedral PO_4^{3-} unit can fill space more efficiently. In a competing second - and slow - reaction step, pyrophosphate anions are formed in a condensation reaction. No pyrophosphates are formed at higher carbonate contents. High strain leads to such a large energy barrier that any reaction is suppressed. Our findings aid in the understanding of the mechanochemical amorphization of calcium carbonate and emphasize the effect of impurities for the stabilization of the amorphous phase. This allowed the synthesis of a new ACC defect variant containing the unique HCO_3^- anion. Our approach outlines a general strategy to obtain new amorphous solids for a variety of carbonate/phosphate systems that offer promise as biomaterials for bone regeneration.

INTRODUCTION

Mechanochemistry has become a tool for the synthesis of new inorganic,[1,2] organic,[3,4] and metal–organic compounds.[5] The product range can be extended by using small amounts of solvents or dispersants (liquid-assisted grinding),[6] ionic compounds (ion- and liquid-assisted grinding),[7] or polymers (polymer-assisted grinding) during grinding.[8] Ball-milling is an established strategy for producing out-of-equilibrium structures, and it can be employed for breaking down bulk materials to nano-size.[9,10] Defect formation on a large scale leads to an amorphization of crystalline solids.[11] Elemental germanium[12] or zeolites[13–15] show a loss of crystallinity during ball-milling, and changes of extended hydrate networks have been reported for $Co_3(PO_4)_2 \times 8\ H_2O$.[16] Ball milling can induce an alloying of metals[17] or polymorph changes (e.g., a transformation from the anatase to the rutile phase of TiO_2).[18] Similarly, organic compounds mixtures of organic and inorganic compounds[19,20] undergo structural changes during mechanochemical treatment. This is of particular interest for pharmaceuticals as the higher solubility of amorphous phases enhances the uptake of drugs with poor water solubility.[21,22] Mechanochemistry is of particular interest for large applications due to its scalability and the reduced use of solvents, which make it a "green chemistry" technique.[23]

Continuous mechanical stress during ball milling was proposed to trigger unusual reactivity and lead to the formation of transient phases that are different from those accessible in conventional solid state reactions.[24] There is limited evidence for or against this hypothesis. *Ex situ* studies,[25,26] where the reactants are converted and analyzed after the reaction, provide little information about intermediates, kinetics and dynamics during the mechanochemical reaction itself. *In situ* measurements, on the other hand, can provide real-time insight into a ball milling environment.[27–31] Time-resolved X-ray diffraction with synchrotron radiation (PXRD) is the method of choice for elucidating chemical reaction pathways by the structure

determination of intermediates whose existence might be deduced only indirectly otherwise. Diffraction, however, provides meaningful information only for crystalline materials. Non-crystalline solids elude structural analysis with diffraction methods. Only local probes, such as vibrational (IR, Raman) and nuclear magnetic resonance (NMR) spectroscopy or total scattering[15,19] can aid in the structural analysis. Since solid state transformations are typically diffusion limited and therefore comparatively slow, a step by step analysis can be used to identify transient phases, where "snapshots" are taken at different stages of the reaction.[34,35] We demonstrate the utility of this approach by unravelling the structure of non-crystalline intermediates from the mechanochemical reaction of calcium carbonate ($CaCO_3$) and calcium hydrogenphosphate (monetite, $CaHPO_4$).

Calcium carbonate is an important biomineral in ascidians and molluscs, and calcium phosphate is an essential constituent of vertebrate hard tissues (bone, dentine, enamel).[36–38] The corresponding amorphous polymorphs play a prominent role in biomineralization.[37,39–42] The transition from amorphous to crystalline phases allows Nature to exert control through ion concentrations (with ion pumps) and organic matrices or molecules.[43] Many research groups have invested substantial efforts to achieve a deep understanding of the mechanism of biomineralization.[44] An application-oriented result of the crystallization mechanisms is the use of amorphous calcium carbonate and phosphate for bone grafting materials or nanocomposites.[45–49] There is a growing interest on the effect of impurities in the local structure of amorphous calcium carbonate (ACC)[50,51] and amorphous calcium phosphate (ACP).[52] Organisms control the metastability of ACC by incorporating additives (like Mg^{2+}, PO_4^{3-} or water).[52] These impurities have strong effects on the local structure of ACC and ACP, and several studies have been carried out to investigate the effect of additives such as magnesium and phosphate ions on ACC.[49–52]

The local structure in ACC is a matter of debate.[53] A "protostructuring" of ACC with respect to different crystalline $CaCO_3$ polymorphs has been proposed,[54,55] and the concept of "polyamorphism" has been considered for biogenic ACC.[53] Although the short-range order in ACC is pH dependent[56] and OH^- groups were found to be incorporated in ACC,[57] there are no indications for the presence of hydrogen carbonate (HCO_3^-) ions in ACC or any hydrated $CaCO_3$ polymorph.[58–61] The synthesis and stabilization of ACC have been pursued by freeze-drying,[62] with polymers[63] and proteins,[64] or foreign ions like Mg^{2+} [65] and phosphate.[52] These approaches start from the Ca^{2+} and CO_3^{2-} ion constituents in aqueous solution, and the crystallization process is stopped at the ACC stage by stabilizing the product kinetically.

Mechanochemical treatment of calcium carbonate has been a topic of previous research. The transformation of calcite to its high-pressure polymorph aragonite has been reported in a mechanically operated mortar.[66] The reverse transformation from aragonite to calcite, the thermodynamically stable polymorph, was described later.[67] Likewise, vaterite can be transformed to calcite mechanochemically.[68,69] In an earlier study we have shown that amorphous $CaCO_3$ could be prepared by ball milling only, when Na_2CO_3 (minimum 7.5 mol %) was added to stabilize the metastable ball-milled amorphous calcium carbonate phase (BM-ACC) by cationic defects.[70] It was, however, not possible to obtain other amorphous alkaline earth metal carbonates for metals other than Ca (e.g. Sr and Ba) by cation "doping" with Sr and Ba. Here we show that amorphous alkaline earth carbonates, in particular amorphous calcium carbonate/calcium hydrogen phosphate (aCCP), amorphous strontium carbonate/calcium hydrogen phosphate (aSCP) and amorphous barium carbonate/calcium hydrogen phosphate (aBCP) can be stabilized by mechanical treatment of crystalline alkaline earth metal carbonates (M = Ca, Sr, Ba, Scheme 1) with $CaHPO_4$.

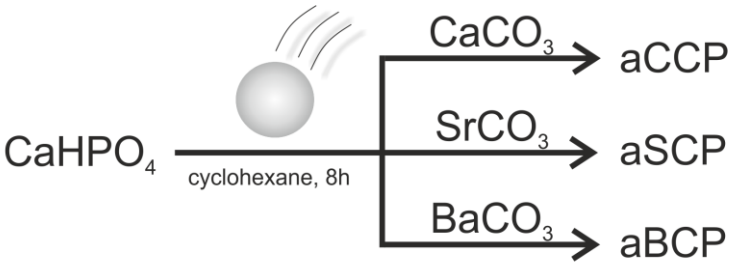

Scheme 1 | Summary of the ball-milling experiment

Different compositions of the starting materials were ground in a high-energy planetary ball mill. The amount of monetite was kept constant (1 mmol) and mixed with different amounts of earth alkali carbonates. The composition of the product is expressed in terms of the mole fraction x(carbonate) = n($CaCO_3$)/(n($CaCO_3$)+n($CaHPO_4$)) (*e.g.* aCCP (0.2): 1 mmol $CaHPO_4$ and 0.25 mmol $CaCO_3$, i.e. x(carbonate)=0.2). Static spin echo delay NMR measurements revealed that even small mole fractions (x = 0.05) cause large structural changes.

The process of amorphization was studied *ex situ* using solid-state nuclear magnetic resonance (ssNMR) spectroscopy and Fourier transform infrared (FTIR) spectroscopy. The local structure of the amorphous compounds was probed by ssNMR spectroscopy. Complementary structural information about the local structure motifs revealing the coordination sphere for the alkaline earth cations was derived from the analysis of total scattering data using synchrotron radiation. The molecular dynamics was derived from X-ray photon correlation spectroscopy (XPCS). An outstanding feature of the amorphous phases is their extraordinary stability

and slow crystallization (up to several months). This is very unexpected as ACC and BM-ACC crystallize within minutes in contact with humidity.[46,71,72] The evaluation of the XPCS data indicates the presence of a highly-strained system in BM-aCCP.

In the first - and fast - reaction step the carbonate anions are protonated by the hydrogen phosphates groups. The formation of hydrogen carbonates (HCO_3^-) and orthophosphates (*i.e.* higher Coulomb energy, the tetrahedral unit can fill space more efficiently) appears to be the driving force of the reaction. This rearrangement reaches mechanochemical equilibrium quickly. In a second reaction step, pyrophosphate anions are formed in a condensation reaction, which competes with proton transfer. Although the energy balance of pyrophosphate formation from two equivalents of hydrogen phosphate ($2HPO_4^{2-} \rightarrow P_2O_7^{4-} + H_2O$) may not be strongly disfavored, the kinetics is slow. No pyrophosphates are formed at higher carbonate contents. Strain due to hydrogen-bonded HCO_3^- groups leads to a large energy barrier that suppresses any reaction.

RESULTS AND DISCUSSION

Ball Milling Reaction

The milling process was monitored *ex situ* using ^{1}H- and ^{31}P- single pulse excitation (SPE) magic angle spinning solid-state nuclear magnetic resonance spectroscopy (^{31}P-MAS-ssNMR) at 10 kHz and FTIR spectroscopy. The full width at half maximum (fwhm) of the NMR signals in crystalline solids is a sensitive measure of the uniformity of the local field[73] and thus suitable to follow the changes during the amorphization process. The milling process of amorphous calcium carbonate/calcium hydrogen phosphate (aCCP 0.2) was stopped after 10 min, 30 min, 60 min, 240 min and 480 min.

Fig. 1a shows the ^{31}P-MAS-ssNMR spectra of aCCP 0.2 as a function of milling time. During the first 30 minutes of milling the two phosphorous resonances at -1.62 and -0.34 ppm are broad but can still be detected. These singals are associated with two different crystallographic environments of the phosphate ion in crystalline $CaHPO_4$. For longer milling times, signal broadening increases due to a loss of crystalline order. The two individual resonances merge indicating complete amorphization. During the milling process the signal shifts to lower field. After 8 h of milling the resonance becomes asymmetric with a maximum at ~ 3 ppm and a broad shoulder at ~ –10 ppm. The appearance of this shoulder indicates the existence of another process besides amorphization.

The same trend was observed in the ^{1}H-MAS-ssNMR spectra (Fig.1b). The ^{1}H spectrum of crystalline monetite displays three ^{1}H resonances at 12.55, 13.22 and 15.60 ppm associated

with different environments of the hydrogen phosphate proton. After 10 min of milling time four additional "solvent" signals can be detected in the ^{1}H spectrum: The signal (i) at 1.22 ppm can be assigned to the presence of the cyclohexane as dispersion medium, (ii) the signal at 4.8 ppm

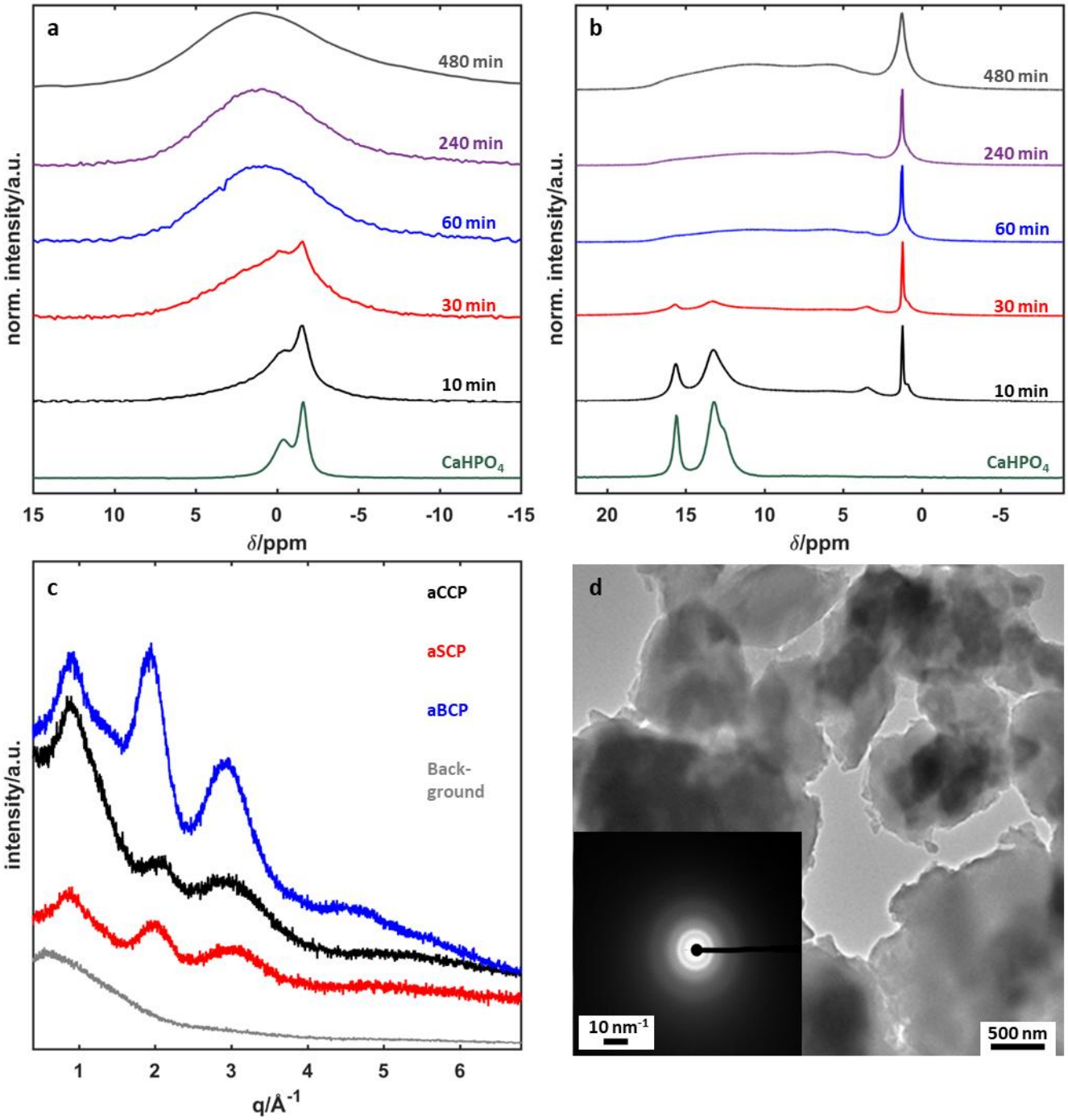

Fig. 1 | (a) ^{31}P-MAS-ssNMR spectra of aCCP 0.2 as a function of milling time in comparison to crystalline $CaHPO_4$. (b) ^{1}H-MAS-ssNMR spectra of aCCP 0.2 as a function of milling time in comparison to crystalline $CaHPO_4$. The ^{1}H spectrum of crystalline $CaHPO_4$ contains three ^{1}H resonances at 12.55, 13.22 and 15.60 ppm related with different environments of the hydrogen phosphate group. After 10 min of milling solvent signals (1.22 ppm: cyclohexane, 4.8 ppm: water, 0.88 and 3.52 ppm: ethanol) appear. The signals broaden with milling time. The broad resonance at 11 ppm (8 h) corresponds to a chemical reaction. (c) X-ray powder diffractograms (XRPD) of aCCP 0.5 (black), aSCP 0.5 (red), aBCP 0.5 (blue) after 480 min of milling time. Background meas-

urement is presented in grey. (d) TEM image of aCCP 0.5 and the associated diffraction pattern after 480 min of milling show complete amorphization.

shows the presence of residual water and (iii) the signals at 0.88 and 3.52 ppm are related to ethanol used in the washing step. These resonances remained unaffected even after drying the sample for 8 h at 40 °C in a vacuum oven (Fig. S1, Supporting Information). This indicates that the solvent molecules are encapsulated in microcavities of the amorphous structure. Increasing the milling time leads to broadening of all signals, related with a loss of order and/or mobility. The appearance of a broad resonance at 11 ppm after 8 h of milling is attributed to changes in the ^{1}H environment leading to higher shielding of the phosphate proton or to a chemical reaction.

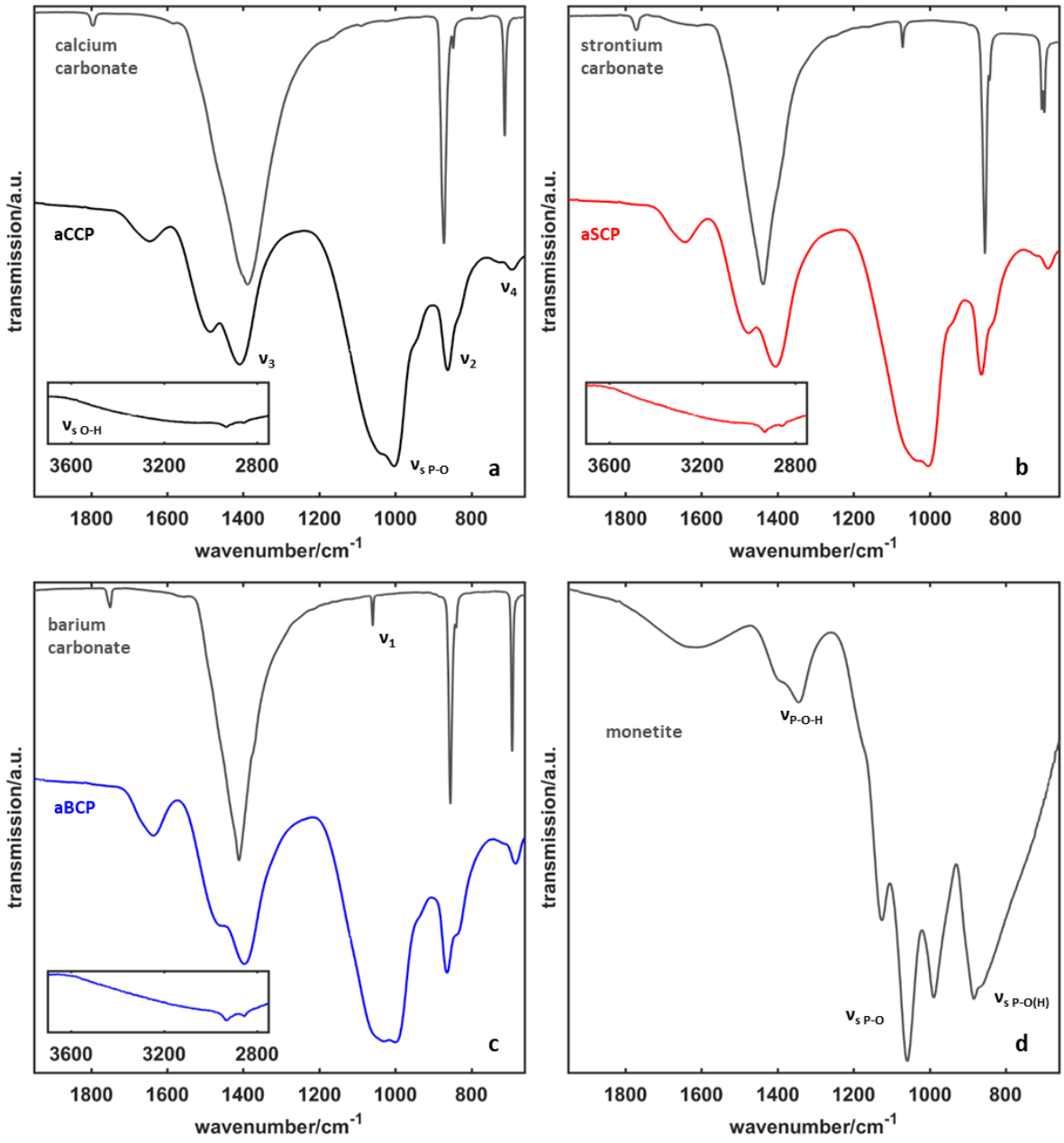

Fig. 2 | IR spectra of crystalline alkaline earth carbonates and ball-milled amorphous alkaline earth carbonate phosphates ($x_{Carbonate}$ = 0.5) after 480 min of milling time. (a) M = Ca, (b) M = Sr, (c) M = Ba. (d) IR reference spectrum of $CaHPO_4$ (monetite).

Fig. 1c shows the X-ray powder diffractograms (XRPD) of the amorphous alkaline earth metal carbonate phosphates (x(carbonate)= 0.5) after 480 min of milling. The loss of all reflections associated with the starting crystalline components and the simultaneous appearance of modulations characteristic for amorphous materials reveal all samples to be "X-ray amorphous". However, the pure starting materials, MCO_3 (M = Ca, Sr, Ba) and $CaHPO_4$, cannot be amorphisized completely by ball milling (exemplary for $CaCO_3$ Fig. S2a, Supporting Information as well as the Quantification of the remaining crystalline proportion: Table S1). Transmission electron microscopy (TEM) images and the associated diffraction patterns for aCCP 0.5 confirm the complete lack of long-range order. The morphology of the particles (Fig. 1d) is very different compared to amorphous carbonates precipitated from solution,[74] and the particles have much larger diameters (up to 1 μm, TEM images of aSCP and aBCP 0.5: Fig. S3, Supporting Information.

Crystalline starting compounds and amorphous products

Fig. 2 shows FTIR spectra of amorphous alkaline earth metal carbonate phosphates ($x_{Carbonate}$ = 0.5) with their respective crystalline precursors. All samples show the characteristic vibration modes of the carbonate ion in amorphous solids,[75,76] in particular for aCCP 0.5: $\nu_2 \approx 862$ and 836 cm^{-1}, $\nu_3 \approx 1410$ and 1493 cm^{-1}, $\nu_4 \approx 693$ and 728 cm^{-1} (Fig. 2a). The expected ν_1 mode of the carbonate ion overlaps with the P-O stretch ($\nu_{s\ P\text{-}O} \approx 1010$ cm^{-1}). Overall, the FTIR spectra of the samples are similar (Fig. 2a-c). Therefore, we expect that the mechanism leading to amorphization is independent of the cation. However, the different Pearson hardness[77] of the alkaline earth cations (absolute values for Mg^{2+}: η=32.5; Ca^{2+}: η=19.7; Ba^{2+}:η=12.8) leads to slight shifts in the ν_2 vibration mode to higher wavenumbers and to lower wavenumbers for the ν_3 and ν_4 vibration modes, which is consistent with the size of the cations. Therefore, the different charge density of the cations leads to different ionic bond strengths, and bands appear at different positions (*i.e.* vibrational energies, Table S1, Supporting Information).

For crystalline monetite the bands of the $\nu_{s\text{-}POH}$ vibrational in-plane bending mode at 1348 and 1401 cm^{-1} overlap with the ν_3 carbonate band (Fig. 2d).[78] Surprisingly, the pronounced band of the $\nu_{s\ P\text{-}O(H)}$ stretch at 884.2 cm^{-1} in crystalline monetite cannot be detected in any of the amorphous products. Possible explanations are (i) strong shifts of the absorption maxima, (ii) strong signal broadening, or (iii) loss of intensity due to chemical transformation. Further-

more, the $\nu_{s\text{-}PO}$ stretch remained broadened in all samples, which is well known for amorphous phosphates.[52,79] The broad bands at about 3500 cm^{-1} are assigned to $\nu_{s\ O\text{-}H}$ stretching modes. All spectral bands show a significant broadening due to the loss of long-range order compared to those of the crystalline compounds. The bands at 2931 and 2853 cm^{-1} indicate that the dispersant medium cyclohexane is occluded in the amorphous product. The bands are characteristic for the asymmetric and symmetric C-H stretch of the CH_2 groups in cyclohexane.[80]

Phosphate Environment: ^{31}P NMR Spectroscopy

The ratio between the starting materials $CaCO_3$ and $CaHPO_4$ has a great effect on the structure of the amorphous products (Fig. 3a). The increase of the carbonate content for a milling time of 480 min results in a shift of the ^{31}P signal of the amorphous product to lower field. For carbonate mole fractions x > 0.3 the maximum of the ^{31}P signal at 1.6 ppm remains unchanged (Fig. 3b). Thus, the average phosphorus environment depends on the milling time (Fig. 1b) and the carbonate:hydrogen phosphate ratio, especially for low carbonate concentrations. For low carbonate contents a shoulder appears at ~ -9 ppm which decreases with increasing carbonate content and disappears almost completely for x = 0.66, i.e. the ^{31}P resonance becomes symmetric.

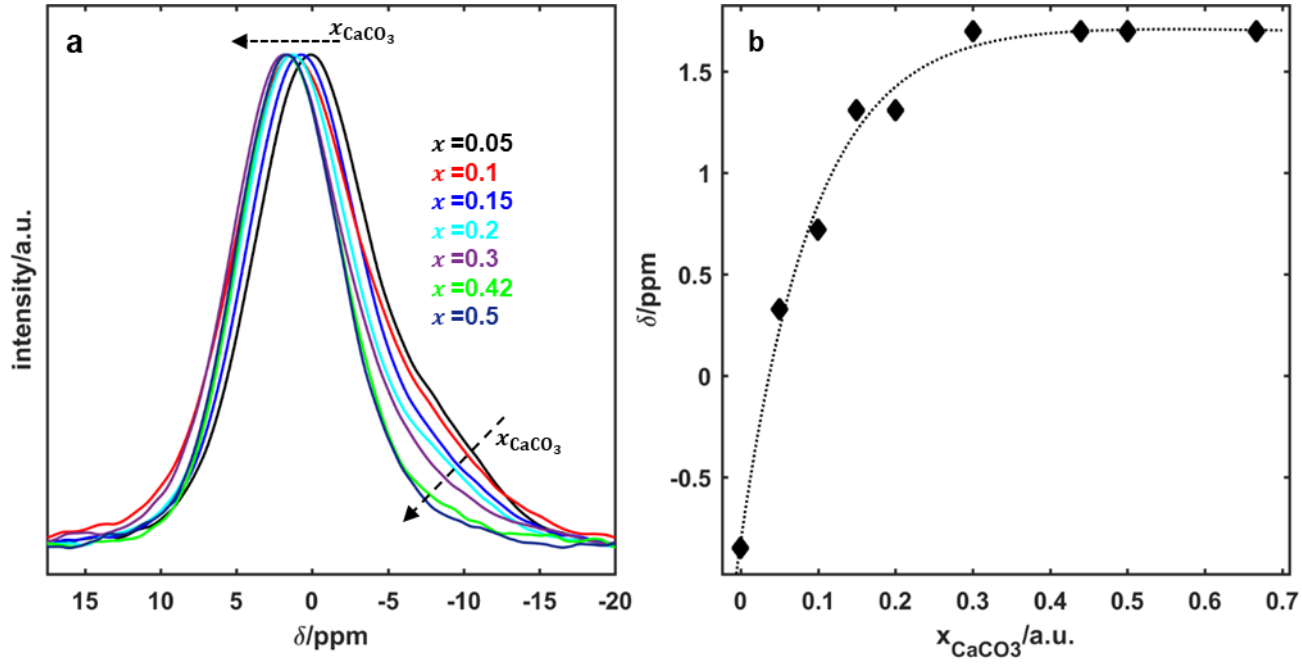

Fig. 3 | (a) ^{31}P signals of ball-milled amorphous calcium carbonate phosphates after 480 min of milling time. (b) Signal maxima of ball-milled amorphous calcium carbonate phosphates as a function of the carbonate mole fraction $x_{Carbonate}$. The ball-milled $CaHPO_4$ after 480 min of ball milling is included additionally.

To further investigate the results of the amorphization process as a function of the carbonate: hydrogen phosphate ratio a TEDOR (Transferred Echo DOuble Resonance) recoupling experiment at 25 kHz MAS was used.[81] The fast magic angle spinning averages the heteronuclear

^{1}H-^{31}P dipole-dipole couplings; this leads to a loss of the associated information. To reintroduce the heteronuclear coupling interaction in the TEDOR experiment, 180° pulses are applied in the middle of the rotor period. The spectra are recorded as a function of the recoupling time (rotor period). Those recorded with short recoupling times provide information about the strongly coupled heteronuclear pairs and those with longer recoupling times reveal information about long range dipolar couplings or about mobile systems where the dipolar interaction is influenced by the motion.

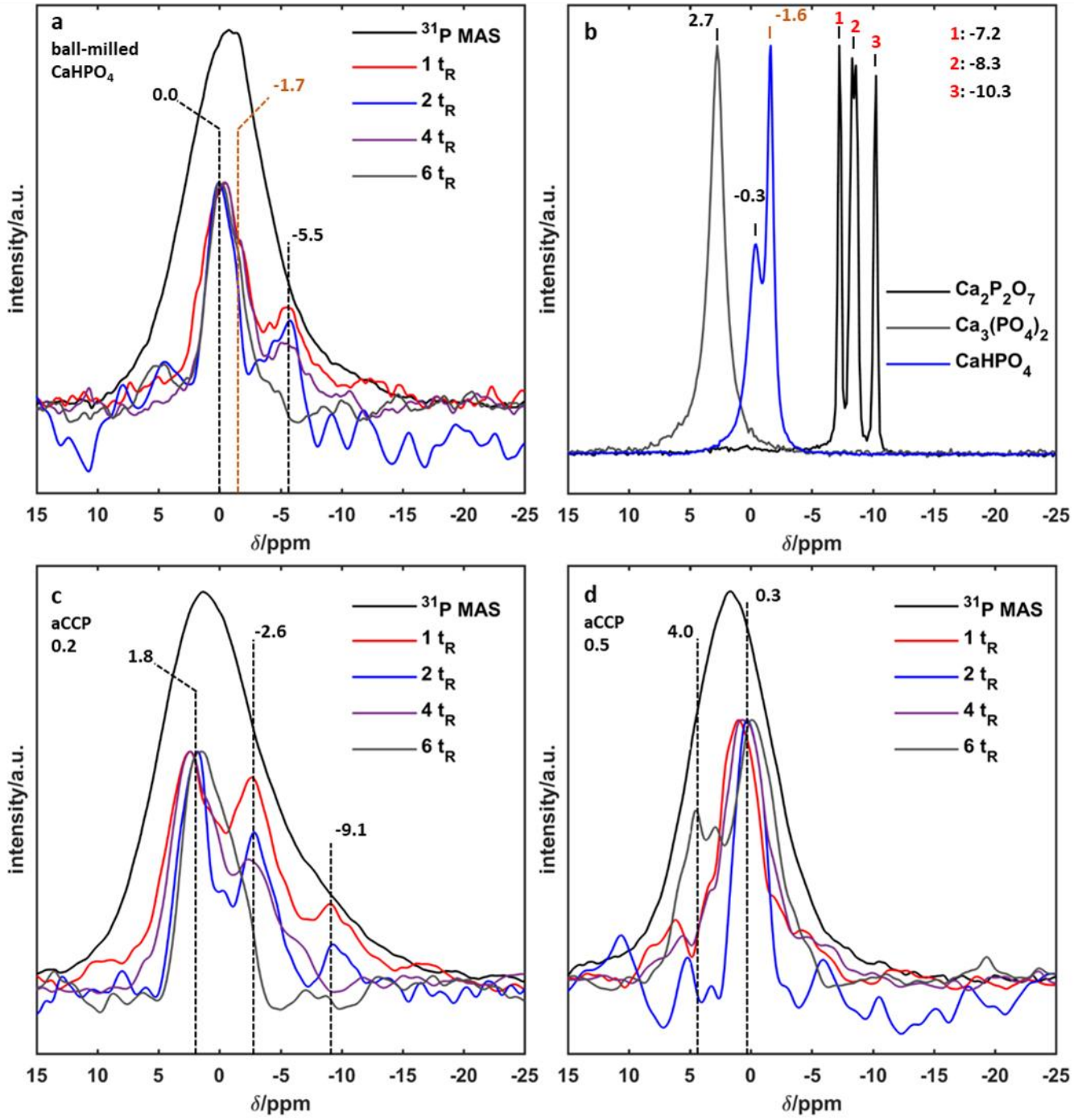

Fig. 4 | (a) ^{1}H-^{13}P TEDOR spectrum of ball-milled calcium hydrogen phosphate, recorded at 1, 2, 4, and 6 rotor periods (40, 80, 160 and 240 µs recoupling time respectively) after 480 min of ball milling. (b) ^{31}P single pulse excitation (SPE) reference spectra of crystalline $CaHPO_4$, $Ca_3(PO_4)_2$ and $Ca_2P_2O_7$. (c) TEDOR spectra of amor-

phous aCCP ($x_{Carbonate}$ = 0.2) after 480 min of ball milling and (d) amorphous aCCP ($x_{Carbonate}$ = 0.5) after 480 min of ball milling as a function of the rotor period, with the respective ^{31}P single pulse excitation (SPE) spectra.

Neutron diffraction studies on crystalline calcium hydrogen carbonate revealed the presence of two crystallographically distinct phosphate groups.[78] At ambient conditions one half of the phosphate groups exist as HPO_4^{2-} with one O-H group covalently bound to the central P atom while the other half has one proton in a symmetrically bridging hydrogen bond and one proton statistically distributed between two centrosymmetric positions.[78,82,83] The existence of two phases – an ordered low temperature and a disordered high temperature phase with a phase transition at about 280 K was suggested.[83] Furthermore, the increased ^{1}H linewidth in low-temperature NMR spectra was assumed to result from a reduced proton mobility.[82] The increased temperature for longer milling times would induce disorder and enhance proton transfer, i.e. destabilize the hydrogen bonds. The applied mechanical force would most probably facilitate the transfer of the protons participating in destabilized hydrogen bonds (orange marked signals at -1.7 and -1.6 ppm, Fig. 4a and b) to different from the original environments (Fig. 4a, signal at -5.5 ppm). This would lead to different phosphorus environments and ^{31}P resonances as observed in the TEDOR spectra (Fig. 4) of the ball-milled calcium hydrogen carbonate phosphate. The ^{31}P signal appearing at ~ -0.3 ppm in the crystalline compound is significantly broadened, but its chemical shift is hardly influenced. On the other hand, the sharp ^{31}P resonance at -1.6 ppm in crystalline $CaHPO_4$ disappears almost completely, and a new signal appears at -5.5 ppm. It may be related with the new environment of the mobile protons and thus lead to different ^{31}P shifts.

Fig. 4a shows a typical ^{1}H-^{31}P TEDOR spectrum of ball-milled calcium hydrogen phosphate, recorded at 1, 2, 4, and 6 rotor periods (40, 80, 160 and 240 μs recoupling time respectively). Reference spectra of crystalline $CaHPO_4$, $Ca_3(PO_4)_2$ and $Ca_2P_2O_7$ are presented in Fig. 4b for comparison. Surprisingly, well defined resonances rather than one broad (amorphous) signal appear in all TEDOR spectra, which implies local order. The ^{31}P SPE reference spectrum is broadened inhomogeneously. In addition, the ^{31}P resonances in the TEDOR spectra (depending on the recoupling time) are shifted by up to 7.5 ppm up- and downfield with respect to the signals for crystalline $CaHPO_4$. These differences - not typical for a simple amorphization - are associated with changes in the chemical (and electronic) environment of the phosphorus atoms when new bonds are formed.

In the TEDOR spectra of the aCCP sample ($x_{Carbonate}$ = 0.2) (Fig. 4c) three resonances appear at 1.8, -2.6 and -9.1 ppm together with a shoulder at ~ -5.5 ppm. The broadened ^{31}P signal at -9.3 ppm and the shoulder at -5.5 ppm are in harmony with the shift range typical for crystalline $Ca_2P_2O_7$.[84] Thus, it is likely that pyrophosphate was formed as an intermediate in a con-

densation reaction during the ball milling process. The other ^{31}P shifts are compatible with hydrogen phosphate or orthophosphate units from the reference spectra. A higher calcium carbonate content (aCCP = $x_{Carbonate}$ = 0.5) (Fig. 4d) results in a loss of the signal at -9.1 ppm. All other resonances in the TEDOR spectra are shifted to lower field (i.e. at 0.3, ~2 and 4.0 ppm). By "diluting" the phosphate starting compound with carbonate the mean P–P distance increases, and a condensation reaction is less likely. In addition, new signals appear at low field, in agreement with the results of the ^{31}P-MAS ssNMR experiments (Fig. 3b). Fig. S4-8 (Supporting Information) summarize the results of the ^{31}P NMR and TEDOR experiments for x = 0.2 and 0.5 for different alkaline earth metals.

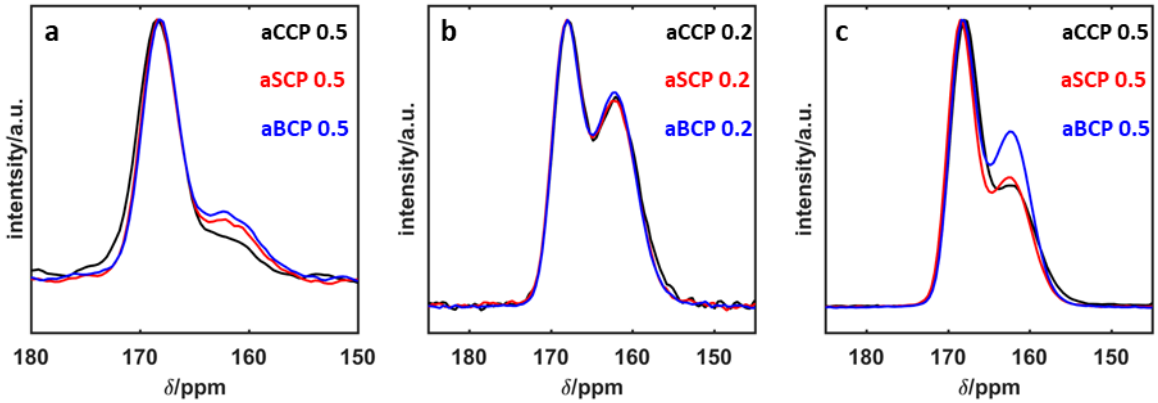

Fig. 5 | (a) SPE ^{13}C NMR spectra and (b) ^{13}C CP NMR spectra of aMCP (M = Ca, Sr, Ba) ($x_{Carbonate}$ = 0.2, t_{cp}= 2ms) and (c) ^{13}C CP NMR spectra (($x_{Carbonate}$ = 0.5, t_{cp}= 2ms) (all spectra: 480 min of ball milling).

Carbonate Environment: ^{13}C NMR Spectroscopy

Ball milling leads to pronounced changes in the ^{31}P environments. The ^{13}C environment was probed as a function of the carbonate content and the alkaline earth metal using ^{13}C SPE, cross-polarization (CP) and heteronuclear correlation (HETCOR) NMR experiments, where two different types of nuclei are correlated *via* through-space dipole-dipole couplings. Fig. 5a shows the SPE ^{13}C NMR spectra for aCCP, aSCP and aBCP ($x_{Carbonate}$ = 0.2)). Fig. 5b presents the corresponding ^{13}C CP NMR spectra and Fig. 5c the ^{13}C CP NMR spectra ($x_{Carbonate}$ = 0.5 content). Two broad resonances appear in all spectra. The first signal at ~168 ppm (full width at half maximum (fwhm): 436 Hz) is typical for amorphous carbonates. The width at half maximum decreases for strontium (aSCP: 390 Hz) and barium ion (aBCP: 379 Hz). This reflects the least ordered local environment in the case of aCCP with decreasing order in the order Ba > Sr > Ca.

The second broad resonance appears at ~162 ppm. Such chemical shifts have been reported by Nebel *et al.*[75] for sodium and potassium hydrogen carbonate. Although the existence of alkaline earth metal hydrogen carbonates is well known in solution,[85–87] there are no reports

about alkaline earth metal hydrogen carbonate in the solid state. This is assessed from this resonance which is associated with the hydrogen carbonate chemical environment. Therefore, in line with the data of the ^{31}P NMR, it can be envisioned that (i) the carbonate group is protonated in an acid/base reaction by the hydrogen phosphate group or (ii) that this specific "hydrogen carbonate" (bicarbonate) environment is formed by reorganization during the milling process. The ^{13}C SPE spectra show a 7:1 ratio between the signals of amorphous calcium carbonate and the hydrogen carbonate. The hydrogen carbonate content in the samples increases drastically for the heavier group homologues $SrCO_3$ (2.6:1) and $BaCO_3$ (2.4:1). The fwhm for the resonance at ~162 ppm is 549 Hz for aCCP, 690 Hz for aSCP, and 703 Hz for aBCP. This correlates well with the increasing ionic radii of the alkaline earth metals (r(Ca^{2+}) = 99 pm; r(Sr^{2+} = 113 pm; r(Ba^{2+}) = 135 pm).[88]

The fraction of the hydrogen carbonate signal is significantly higher for samples with low mole fractions of calcium carbonate. To obtain more information about the distances between the protons and the carbonate group in the different samples, 2D HETCOR NMR spectra were recorded.

Fig. 6 shows prototypical ^{1}H-^{13}C HETCOR spectra of aCCP 0.5 recorded with contact times of 50 and 2000 μs. The spectra of aSCP and aBCP are displayed in Fig. S9 and S10 (Supporting Information). The HETCOR spectrum recorded with a contact time of 50 μs (short range contacts) reveals correlations between the proton signal at 12.2 ppm (bicarbonate) and the signal at 162 ppm (Fig. 6c). Long range contacts due to the heteronuclear dipole-dipole couplings are displayed in the HETCOR experiment recorded with 2000 μs contact time. Correlation between the ^{13}C resonances and protons with a shift in the range of the entrapped solvents (especially cyclohexane) appear additionally in the spectrum (4 ppm).

The spectra with short contact times allow different proton environments around the ^{13}C nuclei and thus the carbonate ions to be resolved. The signal of the amorphous carbonate species at 168 ppm correlates strongly with a proton signal of 15.6 ppm (Fig. 6b). This signal can be assigned to protons of hydrogen phosphates. In contrast, the signal of the hydrogen carbonate species at 162 ppm correlates weaker with the hydrogen phosphate signal. Furthermore, an additional proton signal at 12.4 ppm appears, which can be assigned to the hydrogen carbonate species. This is an indication that unreacted hydrogen phosphates enclose carbonate ions and hydrogen carbonate ions are surrounded by orthophosphate ions. This assumption becomes even more evident in the HETCOR spectra of aSCP and aBCP due to the higher hydrogen carbonate content (see Supporting Information).

The spectra with long contact times additionally reveal ^{1}H signals in the range of the entrapped solvents (especially cyclohexane). Therefore, the heteronuclear dipole-dipole coupling reaches to ^{1}H atoms of entrapped solvents in the grain boundaries.

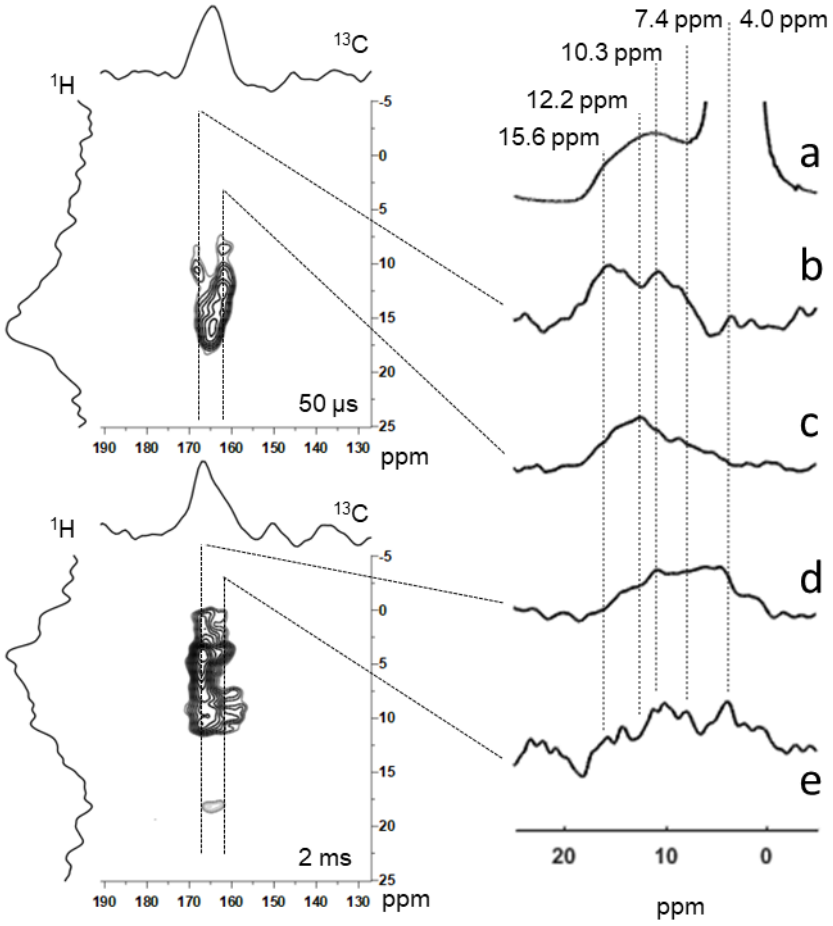

Fig. 6 | ^{1}H-^{13}C HETCOR spectra of aCCP ($x_{Carbonate}$ = 0.5) recorded with contact times of 50 and 2000 µs and respective projections, in particular (a) ^{1}H SPE spectra, (b) projection at 168 ppm with contact times of 50 µs, (c) projection at 162 ppm with contact times of 50 µs, (d) projection at 168 ppm with contact times of 2 ms, (e) projection at 162 ppm with contact times of 2 ms.

Chemical Transformations during Ball-Milling: FTIR Spectroscopy

FTIR spectroscopy provides complementary information to solid state NMR spectroscopy on the chemical transformations of $MCO_3/CaHPO_4$ (M = Ca, Sr, Ba) during ball-milling. ^{13}C enriched samples of aMCP (M = Ca, Sr, Ba) were used to facilitate the assignment of the carbonate or phosphate bands in the FTIR spectra. The higher mass of the ^{13}C isotope shifts the carbonate bands to lower wavenumbers.[89] The difference between samples containing carbon in natural abundance and enriched with ^{13}C is displayed for aCCP for milling time of 480 min in Fig. 7. The difference spectrum shows the bands assigned to (or affected by) the carbonate vibration modes. Particularly relevant are the bands at ~1640 and 850 cm^{-1}. The first is related

to the $(HO)CO_2$ stretch.[90,91] Since the ν_2 (out of plane) mode of the carbonate ion is not degenerate, the associated band splits in two sub-bands. One of them at 862.7 cm^{-1} can be assigned to the amorphous calcium carbonate environment, the one at 828.2 cm^{-1} is associated with calcium hydrogen carbonate. Fitting the FTIR spectra for aCCP 0.5 revealed a ratio of 7:1 for the amorphous and hydrogen carbonate species (see Fig. S11, Supporting Information) which perfectly matches the results from ssNMR. Unfortunately, a similar comparison was not possible for aCCP ($x_{Carbonate}$ = 0.2) due to the overlap with the $\nu_{s\ P\text{-}O(H)}$ stretch at 884.2 cm^{-1}.

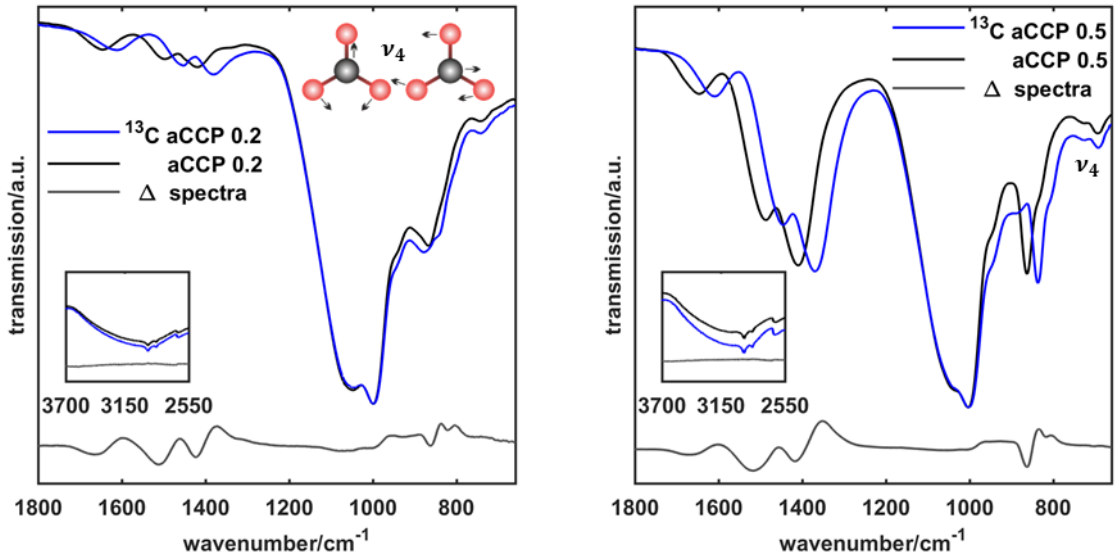

Fig. 7 | Difference spectra of aCCP (a) with $x_{Carbonate}$ = 0.2 and (b) with $x_{Carbonate}$ = 0.5 enriched with ^{13}C and with C in natural abundance for aCCP. The spectra show the essential bands at ~1640 and 850 cm^{-1} assigned to (or influenced by) the carbonate vibrations. The visualized ν_4 vibration mode shows that the carbon atom has only a small influence on the position of these bands.

The FTIR spectra confirm a proton transfer reaction associated with the formation of a chemical bond (HCO_3^-) during ball-milling according to:

$$CaCO_3 + CaHPO_4 \rightarrow (HCO_3)^- + (CaPO_4)^- + Ca^{2+}.$$

Replacement monetite by tricalcium phosphate did not lead to complete amorphization (Supporting Information S2b). Thus, *proton transfer is crucial for the amorphization.* Remarkably, alkaline earth hydrogen carbonates in solid-state have not been reported so far although they are quite common in solution. Pyrophosphates were detected for aCCP ($x_{Carbonate}$ = 0.2) based on the band at 750 cm^{-1}. This band disappears for higher carbonate contents, in agreement with the NMR results (*vide supra*). Finally, the ν_4 band at 683 and 727 cm^{-1} in aCCP ($x_{Carbonate}$ = 0.5) shows no ^{13}C-related shift, although it can be clearly assigned to the carbonate ion. An

explanation is that the ν_4 mode is associated with displacements of the oxygen atoms. Therefore it is nearly independent from the mass of the carbon atom.[89]

Structure: ^{31}P - static spin echo experiments

^{31}P - static spin echo experiments were performed for different compositions x of calcium hydrogen phosphate and alkaline earth carbonates. The Hahn spin echo intensity was measured as a function of evolution time to deduce the homonuclear dipole-dipole interaction. At short evolution times (2τ) the normalized intensities were fitted with a Gaussian function to obtain the second moment $M_{P\text{-}P}$ (Fig. S12, Supporting Information):[92–94]

$$\frac{I(2\tau)}{I_o} = \exp - \left[\left(\frac{M_{\mathrm{P-P}}}{2}\right)(2\tau)^2\right] \quad (1)$$

The NMR second moment reflects the strength of the nuclear magnetic dipole–dipole interaction in solids. The second moment is inversely proportional to the sum of all distances between the nuclei of the same kind and can be calculated on the basis of Van Vleck formula:[95]

$$M_{\mathrm{P-P}} = P\left(\frac{\mu_0}{4\pi}\right)^2 \gamma^4 I(I+1)\hbar^2 \sum_j \frac{1}{r_{ij}^6} \quad (2)$$

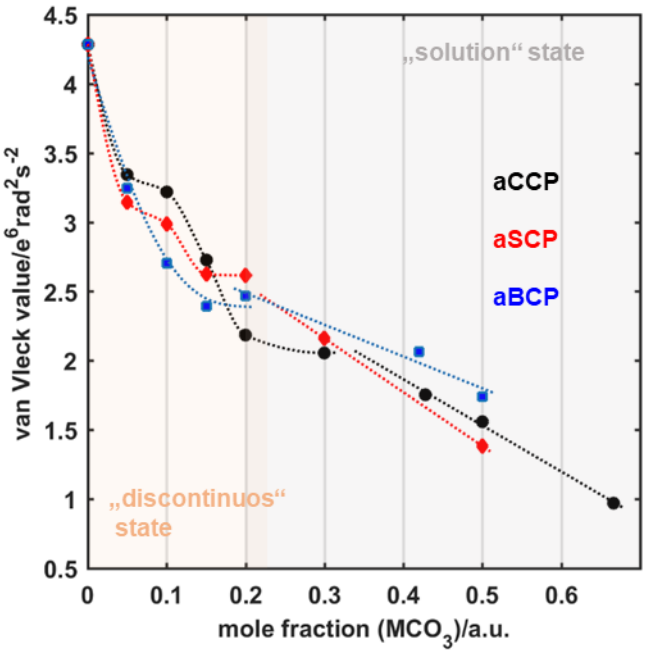

Fig .8 | Second moment of aMCP (M = Ca, Sr, Ba) as a function of composition ($x_{Carbonate}$). ($CaHPO_4$, $x_{Carbonate}$ = 0) has the highest second moment because it is not completely amorphous in the absence of $CaCO_3$. The second moment of crystalline monetite is (for comparison) $4.6 \cdot 10^6\ rad^2 s^{-2}$. The addition small amounts of alkaline earth carbonates lead to a significant decrease of the second moment. The curve is discontinuous, with two steps for calcium and strontium carbonates. This may be rationalized by a chemical reaction (rather than by a physical mixture of the components) for compositions of $x_{Carbonate} < 0.3$. The curve suggests four different processes to occur: (i) Dilution of the phosphates, (ii) condensation reaction to pyrophosphates, (iii) protonation of carbonate and formation of orthophosphates and (iv) increase of the disorder.

Here, γ is the gyromagnetic ratio of the nuclei studied, I the nuclear spin, r_{ij} the internuclear distance, μ_0 the Bohr magneton, and $\hbar$ the Planck constant divided by 2π. Due to the r^{-6} dependence, 90-95 % of the first two coordination spheres contribute to the second moment.[96]

In systems containing abundant magnetically active nuclei of different kind both homo- as well as heteronuclear dipole-dipole couplings are present. Both interactions have an influence on the Hahn echo intensity, however, esp. for amorphous systems containing solvent molecules (in this case water and cyclohexane) these contributions are difficult to evaluate. Thus, our aim is to follow the trend in the Hahn echo signal intensity and relate it with the composition of the mixture of $CaHPO_4$ and earth-alkali carbonates rather than investigating in detail the coupling contributions. Fig. 8 illustrates the dependence of the second moment on the composition of the amorphous alkaline earth carbonate hydrogen phosphate. Monetite shows the highest value of the second moment after mechanochemical treatment because it is not completely amorphous. The second moment of crystalline monetite is (for comparison) with $4.6 \cdot 10^6\ \mathrm{rad^2 s^{-2}}$ only slightly higher. The addition of only 5 mmol of alkaline earth carbonate lead to a significant decrease of the second moment, *i.e.* to a higher average phosphorus-phosphorus distance. The curve has a discontinuous shape with two steps for calcium and strontium carbonates, which can only be explained by a chemical reaction (and not merely by a physical mixture of the components) for compositions up to $x_{Carbonate} = 0.3$. For compositions with $x_{Carbonate} > 0.3$ the behavior is linear, compatible with a solid solution. The shape of the curve suggests four different processes to occur: (i) Dilution of the phosphates, (ii) condensation reaction to pyrophosphates, (iii) protonation of carbonate and formation of orthophosphates and finally (iv) increase of disorder. The curves in Fig. 8 are in good agreement with the results of the ^{31}P MAS and ^{1}H-^{31}P TEDOR NMR experiments. We assume that due to the reaction of hydrogen phosphate to pyro- and orthophosphates the amorphization becomes more favorable.

X-ray total-scattering experiments were performed to probe the local structure of the amorphous products. *GudrunX4* was used to calculate the pair distribution function (PDF) from this data. Fig. 9a shows the PDFs of aCCP 0.5, aSCP 0.5 and aBCP 0.5 with seven significant peaks. The first can be assigned mainly to the phosphorus-oxygen (phosphate ion) distance at 1.52 Å (Fig. 9b: Peak 1). We assume that carbon-oxygen (carbonate ion) distances contribute to this peak as well. This can be explained by the shift of the peak to lower distance values depending on the amount of the starting material calcite and thus a higher ratio of carbonate (aCCP 0.1: 1.54 Å, aCCP 0.2: 1.54 Å, aCCP 0.5: 1.52 Å, aCCP 0.6: 1.50 Å). Further, the decrease of the height of the peak with increasing carbonate amount can be explained by the

higher amount of the carbonate due to its less neighbor atoms compared to phosphate. However, the effective shift is small as the peak is a superposition of both, the P-O as well as the C-O distances, the latter contributing far less (in comparison to synthetic hydrous ACC: 1.25 Å, Fig. S13, Supporting Information) because of the small atomic form factor of both carbon and oxygen which keep the contribution of the C-O pair small. Hoeher et al.[95] reported a C-O distance of 1.3 Å which could also be an explanation for the merged peak. The peak height is not only a measure of the coordination number, but also the total number and product of the atomic form factors.

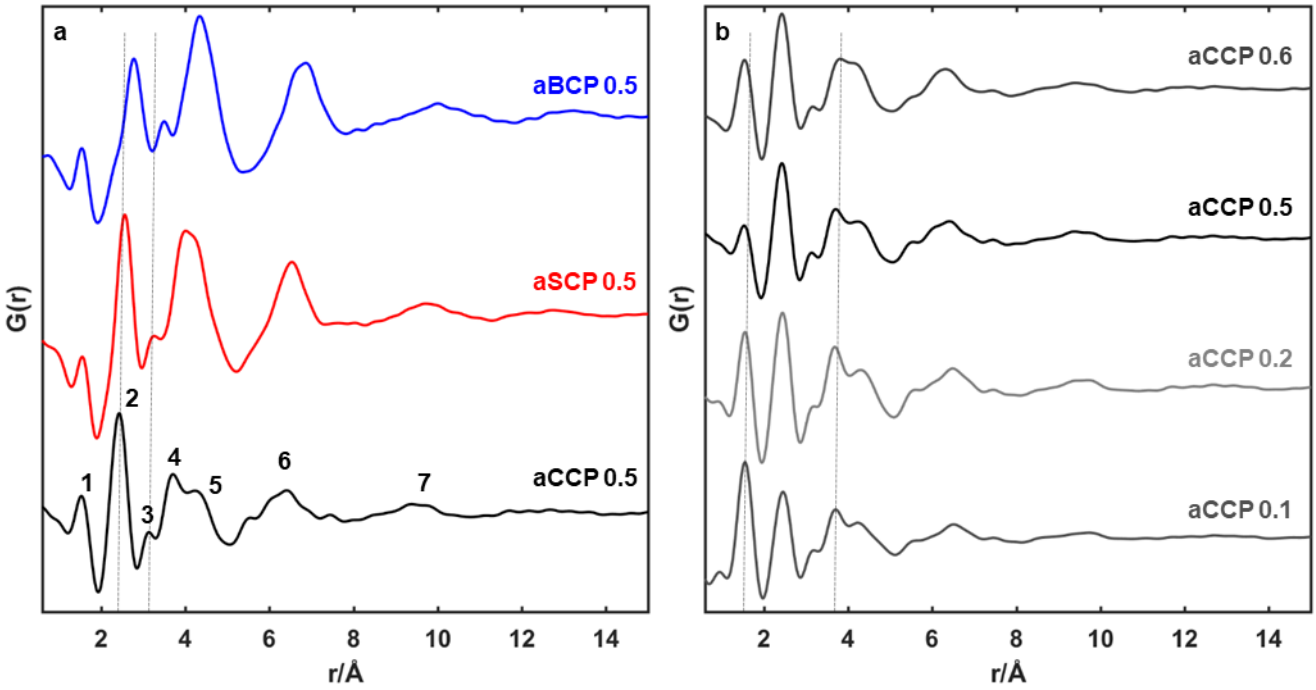

Fig. 9 | Pair distribution function of amorphous products after 480 min of milling: a) Comparison of the PDF data for aCCP (black), aSCP (red), aBCP (blue) x (carbonate) = 0.5. b) Comparison of the PDF data for aCCP with different x(carbonate) = 0.1-0.6. The grey dotted lines highlights the shifts of the peaks.

The most pronounced peak at 2.42 Å for aCCP 0.5 is assigned to the metal-oxygen bonds of the phosphate and carbonate ions. As expected, this peak shifts to higher distances with the larger strontium and barium ions (aSCP 0.5: 2.56 Å and aBCP: 2.78 Å) (Fig. 9a: Peak 2). Note, that this peak, again, is a superposition. The contribution of the molecular O-O pairs of the phosphate ions is low (as above). Further, only for the PDF of aBCP the peaks split due to the Ba-O and Ca-O pairs (due to the mixture of $BaCO_3$ and $CaHPO_4$).

The peak at 3.12 Å for aCCP 0.5 can be assigned most probably to the metal-phosphorus distance (Fig. 9a: Peak 3). Since the peak shifts depending on metal cations, a metal is involved in these pairs (aSCP 0.5: 3.26 Å aBCP 0.5: 3.50 Å). In the next peak at 3.66 Å for aCCP 0.5, phosphorus-metal, phosphorus-phosphorus and metal-metal distances are expected to have a

large contribution (in comparison to crystalline monetite, Fig. 9a: Peak 4).[83] The shift to lower P-P distances compared to crystalline monetite (3.91 Å) indicates changes in the phosphorous coordination sphere and most probably a stressed and distorted system. Furthermore, a variety of different interatomic distances contribute to the higher peaks (4.3 Å, 6.3 Å and 9.42 Å, Fig. 9a: Peak 5,6,7), mainly metal-metal distances. The PDF fade out early and become virtually flat at ~10 Å indicating a total lack of translational coherence. The PDF of aSCP and aBCP are in Fig. S14 (supporting information).

Dynamics of the Amorphous Alkaline Earth Carbonate Hydrogen Phosphates: X-ray photon correlation spectroscopy

X-ray photon correlation spectroscopy (XPCS) is a powerful tool to probe the dynamics of disordered systems, giving information about the rate of structural rearrangements per unit of time (see Supporting Information for further details about data analysis). XPCS experiments yield relaxation curves from which structural relaxation times and shape factors related to the nature of the dynamics (Fig. 10) can be extracted. XPCS confirms the extraordinarily low dynamics in this system, *i.e.* the rate of rearrangements per unit of time is very slow. Values for the structural relaxation time are one to two orders of magnitude higher than those of synthetic hydrous ACC precipitated from solution (see Table 1).[50] Furthermore, and similar to synthetic hydrous ACC, the shape factor β shows extremely high values. In comparison, Brownian molecular motion has a value of one. This is a strong indication for a dynamically highly strained system.[97]

Table 1. Fitted parameters (τ, β) obtained from the intensity auto-correlation functions measured at the start of the experiment, i.e., minimizing the effect of vacuum and related water loss. Relaxation times for the aCCP 0.2 sample cannot be determined precisely, only lower boundary can be established.

Sample	τ (s)	β
aCCP 0.2	>7000	-
aCCP 0.5	756 ± 27	1.69 ± 0.067
aSCP 0.5	1707 ± 133	1.91 ± 0.096
ACC	572 ± 11	1.64 ± 0.041

As discussed by Koishi *et al.*,[50] ACC shows physical aging, *i.e.* τ evolves over time. The same behavior was observed for ball-milled ACC (Fig. 10). This can be explained for ACC by the loss of small amounts (few weight %) of water during the measurement due to an active vacuum. These minor changes in the mass of water cannot be detected by the static structure factor S(q), but they can have a large impact on the dynamics. DTA/TG measurements (Fig.

S15, Supporting Information) showed that ball-milled ACC is almost anhydrous, with water mass losses (temperature range from RT to ~200°C) of <1 % (as opposed to 15-20 % in synthetic hydrous ACC). *Ex situ* measurements for aCCP ($x_{Carbonate}$ = 0.2) and aCCP ($x_{Carbonate}$ = 0.5) with and without these vacuum conditions showed a decrease in the mass loss after exposing the samples to vacuum, confirming the hypothesis for the observed aging of the dynamics under active vacuum (Fig. S16, Supporting Information). The relatively broad band at about 3000 cm^{-1} in the FTIR spectra can be assigned to the O—H stretch of the hydrogen carbonates and hydrogen phosphates ions (with the exception of CH_2-CH_3 stretching bands between 3000-2800 cm^{-1}). The FTIR spectra of the same samples before and after exposure to vacuum show a lower stability to vacuum of the sample aCCP ($x_{Carbonate}$ = 0.2), the spectra of the aCCP ($x_{Carbonate}$ = 0.5) remaining unchanged (Fig. S17, Supporting Information). These complementary observations confirm the observed aging response of each of the samples, with a more pronounced aging for the aCCP ($x_{Carbonate}$ = 0.2) sample (Fig. 10).

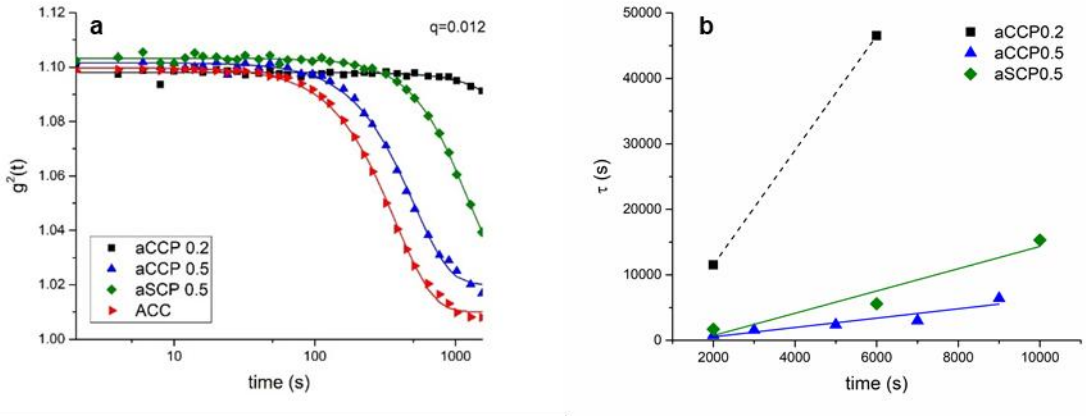

Fig. 10 | (a) Intensity auto-correlation functions at initial experimental time for synthetic ACC prepared from solution (red triangles), aCCP for $x_{Carbonate}$ = 0.2 and 0.5 and for aSCP for $x_{Carbonate}$ = 0.5 at q = 0.012 $Å^{-1}$ (d ≈ 50 nm). (b) Evolution of the relaxation times τ as a function of the experimental time for aCCP for $x_{Carbonate}$ = 0.2 and 0.5 and for aSCP for $x_{Carbonate}$ = 0.5.

DISCUSSION

Reactions and Mechanisms

The ^{1}H-^{13}P TEDOR spectrum (see Fig. 4a) reveals that only the environment of one phosphorous atom in pure $CaHPO_4$ is significantly affected (loss of the ^{31}P resonance at -1.6 ppm) during the ball milling process, whereas the other resonance signal is only broadened. As a result of a condensation reaction, a signal at -5.5 ppm (typical for pyrophosphates) appears in the ^{1}H-^{31}P TEDOR spectrum. Based on the structural and spectroscopy data the following scenario may be derived for the sequence of events in the ball-milling reaction between $CaHPO_4$ and MCO_3 (M = Ca, Sr, Ba) for different ratios $x_{Carbonate}$ (Fig. 11).

The first - and fast - reaction is a proton transfer resulting in a local charge disorder. This forces the system to reorganize. The carbonate anions act in this step as proton acceptors (bases), the hydrogen phosphates act as proton donors (acids). The formation of hydrogen carbonates and orthophosphates (*i.e.* higher Coulomb energy, the tetrahedral unit can fill space more efficiently) appears to be the driving force of the reaction.

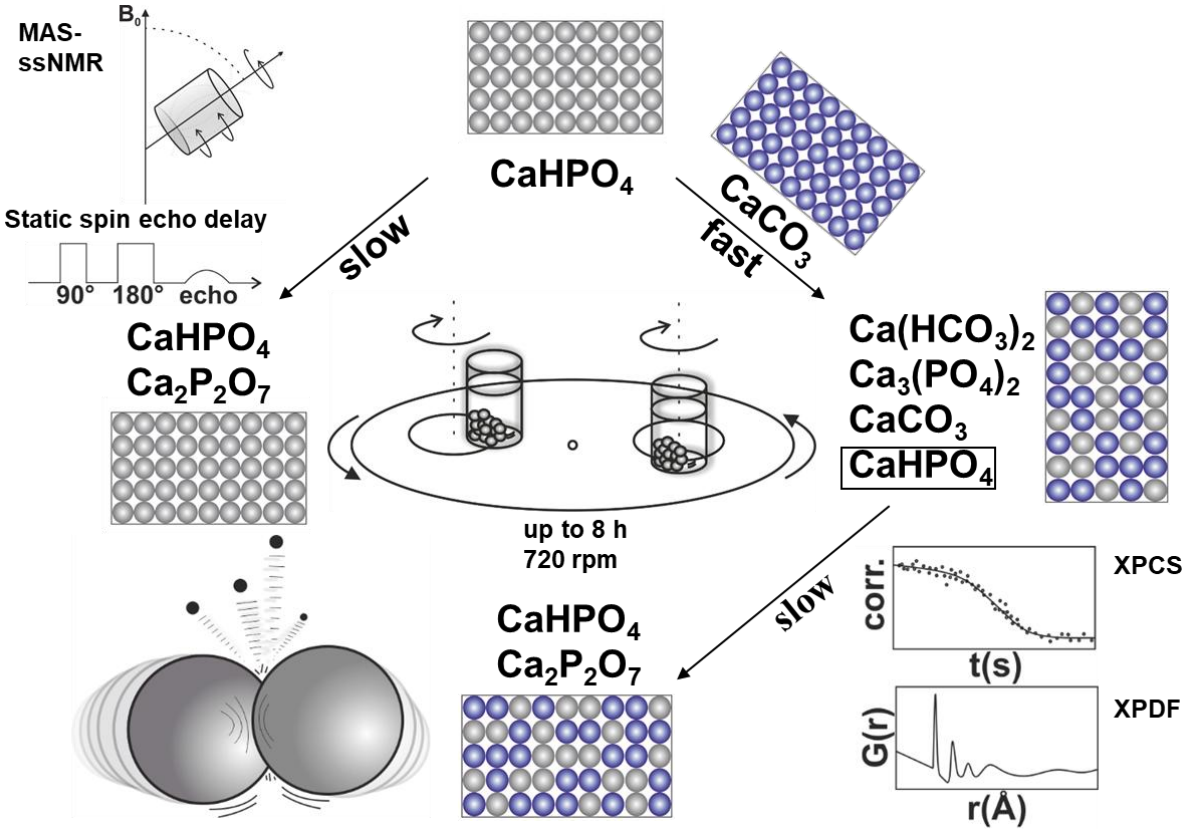

Fig. 11 | Summary of solid state reactions induced by ball-milling of $CaCO_3$ and $CaHPO_4$.

This rearrangement quickly reaches mechanochemical equilibrium. There are two possible reasons for the observed incomplete reaction to hydrogen carbonate. (a) Only the disordered protons statistically distributed between the two positions of the phosphate unit are involved in the reaction, whereas those protons bound covalently to one phosphate group do not react (activation barrier too high). (b) The newly formed structures may be stabilized by strong hydrogen bonds. The proton transfer reaction leads to local charge disbalances which can be compensated by cation motion. The strong hydrogen-bonded network hinders cation motion (the energy of the ball mill is not sufficient to induce cation "jumps"). The result is a highly strained system.

Additionally, a second -and slow - condensation reaction to pyrophosphates occurs, which competes with proton transfer. Although the energy balance of pyrophosphate formation from two equivalents of hydrogen phosphate ($2HPO_4^{2-}$ -> $P_2O_7^{4-}$ + H_2O) may not be strongly disfavored, the kinetics is slow.[98]

It has been suggested that crystalline monetite has an ordered low temperature phase (space group $P1$) and a disordered high temperature phase (space group $P\overline{1}$).[83] A second order phase transition (order/disorder transformation) occurs between 273 and 287 K, where only H positions are significantly affected. Therefore, the disordered phase is present at room temperature with small amounts of the ordered phase. We speculate that in aCCP ($x_{Carbonate}$ = 0.2) H atoms undergo an order/disorder transformation under vacuum conditions. Since this phase transition only affects protons, no difference can be detected in the structure factor. Furthermore, the proportion of monetite in the aCCP ($x_{Carbonate}$ = 0.2) sample is significantly higher.

No pyrophosphates are formed at higher carbonate contents (x(carbonate) > 0.2). Possible reasons are: (i) At higher dilution the mean distance between two HPO_4^{2-} groups (and therefore contact probability and time) decreases. Therefore, it is much less likely that two hydrogen phosphate ions will be able to stay in contact long enough and react. (ii) The formation of orthophosphates (PO_4^{3-}) in the acid-base reaction between CO_3^{2-} and HPO_4^{2-} preceding pyrophosphate condensation leads to an even stronger dilution effect. (iii) The highly-strained system leads to such a large energy barrier that any reaction is suppressed.

Conclusions

In conclusion, we have explored the formation of amorphous anhydrous alkaline earth carbonates in a planetary ball mill. In essence, the phosphate anions stabilize the metastable product through the formation of a highly strained network that hinders recrystallization kinetically. The minimum concentration of phosphate "impurities" for the successful amorphization of calcite was determined by PXRD, ^{31}P and ^{1}H MAS-NMR and electron microcopy. Since diffraction is not suited for studying amorphous solids, the intermediates of the ball-milling reaction were studied by local probes using vibrational spectroscopy, double resonance ^{1}H-^{31}P TEDOR and ^{1}H-^{13}C HETCOR spectroscopy, which are highly sensitive to symmetry changes of the local environment. Mechanistically, CO_3^{2-} anions are protonated *via* an acid-base process by hydrogen phosphate groups in the first - and fast - reaction step of the ball-milling reaction. The concomitant formation of unprecedented hydrogen carbonate (HCO_3^-) anions and orthophosphate groups are the driving force of the reaction, because the phosphate group has a higher Coulomb energy and the tetrahedral PO_4^{3-} unit can fill space more efficiently. In a competing second - and slow - reaction step, pyrophosphate anions are formed in a condensation reaction. No pyrophosphates are formed at higher carbonate contents. The structure and dynamics of the amorphous ball-milled products were studied by vibrational spectroscopy, ^{31}P - static spin echo experiments, pair distribution analysis and X-ray

photon correlation spectroscopy, which show the evolution of the phosphorus environment and the strength of the hydrogen bonded network.

Our findings aid not only in the in the understanding of the mechanochemical amorphization of calcium carbonate and the effect of impurities for the stabilization of the amorphous phase. They shed light on elementary reaction steps during ball-milling reactions which are ubiquitous in pharmaceutical or chemical industry, although a mechanistic understanding required for their development is still lacking. Finally, the ball-milling process allowed the synthesis of a new ACC defect variant containing the unique hydrogen carbonate anions.

METHODS

Materials. Calcite (98%, Socal 31, Solvay), monetite ($CaHPO_4$) (>98.5%, anhydrous, Sigma-Aldrich), $SrCO_3$ (99+%, chempur), $BaCO_3$ (99+%, Sigma-Aldrich), β-Tricalcium phosphate (96+%, Sigma-Aldrich), Strontium chloride (anhydrous, 99.5%, Alfa Aesar), Calcium carbonate-^{13}C (99 atom % ^{13}C, isotec), Sodium carbonate (13C 99%, deutero), Barium carbonate (13C 98%, deutero) , cyclohexane (Analytical reagent grade, Fisher Chemicals), ethanol (absolute 99.8+%, Fisher Chemicals) and milliQ deionized water.

Synthesis of Calcium Pyrophosphate. Loaded in a corundum jar, monetite (7.35 mmol) was heated to 800 °C in a horizontal tube furnace oven for 8 h (5 °C/min). Afterward, the resulting product was grinded.

Synthesis of ^{13}C Enriched $SrCO_3$. $SrCl_2$ (2.1 mmol) was dissolved in 50 mL of deionized water. The solution was degassed with an argon stream for 30 minutes. Under argon atmosphere and vigorous stirring ^{13}C enriched Na_2CO_3 (2 mmol) was added to the solution. The reaction solution was stirred for one hour. Afterward, the precipitate was separated by centrifugation and washed with water and ethanol. The product was dried in vacuo.

Synthesis of Amorphous Earth Alkaline Metal Carbonate Hydrogenphosphates. Monetite (0.136 g, 1 mmol) was treated with different amounts of earth alkali metal carbonates (*e.g.* aCCP 0.5: 0.100 g, 1 mmol) in a planetary ball mill (Pulverisette 7 Classic, Fritsch). The starting materials and 10 mL of cyclohexane were transferred together with 3.65 grams of grinding balls (about 1100 balls, 1 mm diameter, ZrO_2) into ZrO_2 grinding jars. The mixture was milled for certain times at 720 rpm. To avoid overheating, alternate 10 minutes of grinding and then a 10 minute rest phase was used. Therefore, 480 min of ball milling results in 950 minutes of reaction time. Afterward, the cyclohexane was removed with a pipette. The prod-

uct was dispersed in ethanol and separated from the grinding balls by decanting. The product was isolated by centrifugation and dried in vacuo.

Characterization

X-ray Powder Diffraction. X-ray diffractograms were recorded with a STOE Stadi P equipped with a Mythen 1k detector using Mo $K\alpha_1$ radiation (λ=0.7093 Å). The dry samples were prepared between polyvinyl acetate foils in perfluoroether (Fomblin Y, Aldrich). The measurements were performed in the 2θ range from 2° to 45° with a step size of 0.015° (continuous scan, 150 s/deg). Crystalline phases were identified according to the PDF-2 database using Bruker AXS.

ATR-FTIR Spectroscopy. The attenuated total reflection (ATR) FTIR spectra were recorded on a Nicolet iS10 spectrometer (Thermo scientific) using a frequency range from 650 to 4000 cm^{-1} with a resolution of 1.4 cm^{-1} per data point.

Solid-State NMR Spectroscopy. All solid state NMR spectra were recorded on a Bruker Advance 400 DSX NMR spectrometer (Bruker BioSpin GmbH, Rheinstteten, Germany operated by Topspin 1.3, 2007, patchlevel 8) at a ^{1}H frequency of 399.87 MHz, ^{13}C frequency of 100.55 MHz and ^{31}P frequency of 161.87 MHz. A commercial 3 channel 4 mm Bruker probe head at 10 kHz magic angle spinning (MAS) was used for all experiments. The ^{1}H NMR spectra and ^{1}H background corrected spectra were recorded averaging 32 transients with 8 s recycle delay. For all solid-state ^{13}C cross-polarization (CP) magic angle spinning (MAS) NMR experiments, an initial 90° pulse with 4.0 μs length and 5 s recycle delay were used. A ramped CP pulse (from 64 to 100%) with duration of 20 μs, 50 μs, 100 μs, 200 μs, 500 μs, 1 ms, 2 ms, 3 ms, 5 ms and 7 ms was used for recording the CP build-up curves. Two pulse phase modulation (TPPM) ^{1}H decoupling scheme was used while acquiring the ^{13}C signal. 512 transients were averaged for the CP experiments. The spectra were baseline-corrected and a broadening of 30 Hz was applied. Quantitative ^{13}C single pulse excitation experiments allowing full relaxation have been recorded averaging 16 transients with a recycle delay of 2200 s and TPPM heteronuclear decoupling. The spectrum was background corrected and a broadening of 30 Hz was applied. The ^{1}H-^{13}C heteronuclear correlation (HETCOR) 2D NMR spectra were acquired using ^{1}H-^{13}C magnetization transfer with contact times of 50 and 2000 µs and 256 transients/t1. The data points recorded were 1 k (t1) and 96 or 128 (t2) and zero-filled to 4 k (t1) and 256 (t2) before the 2D Fourier transformation. The other parameters were identical to those for the 1D CP NMR experiments. Single pulse excitation ^{31}P experiments

were recorded using 60 s recycle delay averaging 16 scans under TPPM heteronuclear decoupling while acquiring the NMR signal. For all ^{31}P cross-polarization (CP) magic angle spinning (MAS) NMR experiments, an initial 90° pulse with 4.0 μs length and 5 s recycle delay were used. A ramped CP pulse (from 64 to 100%) with duration of 20 μs, 50 μs, 100 μs, 250 μs, 500 μs, 1 ms, 2 ms, 3 ms, 4 ms and 5 ms was used for recording the CP build-up curves. Two pulse phase modulation (TPPM) ^{1}H decoupling scheme was used while acquiring the ^{31}P signal. Transients of 64 were averaged for the CP experiments. The spectra were baseline-corrected and a broadening of 30 Hz was applied. The ^{1}H-^{31}P heteronuclear correlation (HETCOR) 2D NMR spectra were acquired using ^{1}H-^{31}P magnetization transfer with contact times of 20 and 2000 μs and 64 transients/t1. The data points recorded were 2 k (t1) and 128 (t2) and zero-filled to 4 k (t1) and 256 (t2) before the 2D Fourier transformation. The other experimental parameters were identical to those for the 1D CP NMR experiments. All ^{1}H-^{31}P transferred echo double resonance (TEDOR) experiments were recorded averaging 512 scans using TPPM heteronuclear decoupling while acquiring the NMR signal. 1, 2, 4, 6, 8 and 10 full rotor periods (τ_R) were used for recoupling the heteronuclear dipolar couplings corresponding resp. to 40 μs, 80 μs, 160 μs, 240 μs, 320 μs and 400 μs recoupling time. A broadening of 30 Hz and background correction were applied. All static ^{31}P Hahn echo experiments were recorded with echo delays of 30, 40, 50, 60, 70, 80, 90 and 100 μs.[99,100] A broadening of 150 Hz and background correction were applied. The spectra were referenced to external adamantine at 1.63 ppm (^{1}H) and 38.5 ppm (^{13}C) and to external NH_4HPO_3 at 0.9 ppm (^{31}P). Spectral deconvolution and fitting the intensity decrease in the spin-echo experiments were performed using self-written MatLab scripts (version 2017b).

Thermal Analysis. Coupled thermogravimetry-differential thermal analysis (TG-DTA) was carried out at a Netzsch STA 449 F3 Jupiter device. About 10 mg of the sample was heated in an alumina cup in argon atmosphere from 50 to 900 °C at a heating rate of 10 K/min.

Transmission Electron Microscopy (TEM). Samples were prepared by drop-casting 20 μL of the respective sample dispersion on 400 mesh carbon copper grids (Plano GmbH, Wetzlar, Germany) and measured with a Technai Spirit G2 at 120 kV acceleration voltage, equipped with a standard 4K CCD camera.

Total Scattering. Total scattering measurements of amorphous earth alkali metal carbonate hy-drogen phosphates were performed at beamline P02.1 at Petra III, DESY, Germany using an X-ray energy of 60 keV (λ = 0.20724 Å).[101] All samples were prepared in a 0.5 mm borosilicate capillary and measured in transmission mode with a 2D Perkin Elmer area detector with 2048 x 2048 pixels. The exposure time for each sample was 15 min. The resulted 2D

images were integrated by using the program DAWNscience.[102] The analysis of the atomic pair distribution function (PDF) was performed utilizing the Gudrun X software using an empty capillary (0.5 mm) for background subtraction with Qmax = 24 Å-1.[103]

X-ray Photon Correlation Spectroscopy. XPCS experiments were performed at the beam line P10 of PETRA III at DESY synchrotron radiation source at Hamburg (Germany), using an incident energy of Xrays of 15 keV. Samples were prepared by loading the powders into 1 mm diameter holes drilled in ~100 µm thickness Al foils. The hydrated, plastic texture of the sample results in a homogeneous filling of all the space. The ~100 µm thickness ensure a transmission of ~9% at 15 keV. Measurements were performed under active vacuum (of $\sim 10^{-3}$ mbar), covering a 0.007-0.013 $Å^{-1}$ q range (small-angle configuration) and with a beam size of 15×15 µm. Series of speckles patterns were collected in transmission geometry by a CCD detector (Andor, 13 µm pixel size). In order to avoid radiation damage of the sample, a delay time (waiting time between two consecutive frames) of 1.9 s was set after each 0.1 s acquisition. Series of acquisitions were taken for at least 2000 frames, covering relaxation times of several hours. These series of measurements were taken by moving the sample by at least twice the beamsize to avoid exposing the same spot for long time, preventing radiation damage and beam induced dynamics. All measurements were carried out at T = 25°C. Details about the XPCS data analysis are given in the Supporting Information.

Author Information

Corresponding Authors: tremel@uni-mainz.de, mondeshk@uni-mainz.de

Acknowledgements

M.P. A. was supported by the European Union's Horizon 2020 research and innovation programme under the Marie Skłodowska-Curie grant agreement 747597. A.F.-M. acknowledges funding from the Agence Nationale de la Recherche (ANR-JCJC 'NUANCE', ANR-17-CE08-0057). Michael Sprung and Fabien Westermeier (DESY) are thanked for their help during XPCS experiments.

We acknowledge DESY (Hamburg, Germany), a member of the Helmholtz Association HGF, for the provision of experimental facilities. The PDF measurements of this research were carried out at P02.1 and we would like to thank Dr Alexander Schökel for assistance.

Author contributions

N. K. carried out the experiments, L. N. initiated the study, L. N., M. D. and W. T. conceived the experiments, I. L., C. L., M. P. A., A. F.-M., A. D., B. B. and S. L. contributed to meth-

ods, N. K. wrote the manuscript with contributions of L.N., F. N., M. P. A., A. F.-M., A. D, and W. T.

Additional Information

The data (Table S1 and 2, Fig. S1- Fig. S17) that support the plots within this paper and other findings of this study are available from the corresponding authors on request.

Competing Interests

The authors declare no competing financial interest.

References

(1) Šepelák, V., Düvel, A., Wilkening, M., Becker, K.-D. & Heitjans, P. Mechanochemical Reactions and Syntheses of Oxides. *Chem. Soc. Rev.* **42** (18), 7507-7520 (2013). https://doi.org/10.1039/c2cs35462d.

(2) Baláž, P. et al. Hallmarks of Mechanochemistry: From Nanoparticles to Technology. *Chem. Soc. Rev.* 42 (18), 7571-7637 (2013). https://doi.org/10.1039/c3cs35468g.

(3) Boldyreva, E. Mechanochemistry of Inorganic and Organic Systems: What Is Similar, What Is Different? *Chem. Soc. Rev.* **42** (18), 7719-7738 (2013). https://doi.org/10.1039/c3cs60052a.

(4) James, S. L. et al. Mechanochemistry: Opportunities for New and Cleaner Synthesis. *Chem Soc Rev* **41** (1), 413–447 (2012). https://doi.org/10.1039/C1CS15171A.

(5) Garay, A. L., Pichon, A. & James, S. L. Solvent-Free Synthesis of Metal Complexes. *Chem. Soc. Rev.* **36** (6), 846-855 (2007). https://doi.org/10.1039/b600363j.

(6) Bowmaker, G. A. Solvent-Assisted Mechanochemistry. *Chem Commun* **49** (4), 334–348 (2013). https://doi.org/10.1039/C2CC35694E.

(7) Friščić, T. et al. Ion- and Liquid-Assisted Grinding: Improved Mechanochemical Synthesis of Metal-Organic Frameworks Reveals Salt Inclusion and Anion Templating. *Angew. Chem. Int. Ed.* **49** (4), 712–715 (2010). https://doi.org/10.1002/anie.200906583.

(8) Hasa, D., Schneider Rauber, G., Voinovich, D. & Jones, W. Cocrystal Formation through Mechanochemistry: From Neat and Liquid-Assisted Grinding to Polymer-Assisted Grinding. *Angew. Chem. Int. Ed.* **54** (25), 7371–7375 (2015). https://doi.org/10.1002/anie.201501638.

(9) Fecht, H. J., Hellstern, E., Fu, Z. & Johnson, W. L. Nanocrystalline Metals Prepared by High-Energy Ball Milling. *Metall. Trans. A* **21** (9), 2333–2337 (1990). https://doi.org/10.1007/BF02646980.

(10) Annenkov, M. et al. Boron Carbide Nanoparticles for High-Hardness Ceramics: Crystal Lattice Defects after Treatment in a Planetary Ball Mill. *J. Eur. Ceram. Soc.* **37** (4), 1349–1353 (2017). https://doi.org/10.1016/j.jeurceramsoc.2016.12.001.

(11) Weeber, A. W. & Bakker, H. Amorphization by Ball Milling. A Review. *Phys. B Condens. Matter* **153** (1–3), 93–135 (1988). https://doi.org/10.1016/0921-4526(88)90038-5.

(12) Gaffet, E. Phase Transition Induced by Ball Milling in Germanium. *Mater. Sci. Eng. A* **136**, 161–169 (1991). https://doi.org/10.1016/0921-5093(91)90451-R.

(13) Cao, S., Bennett, T. D., Keen, D. A., Goodwin, A. L. & Cheetham, A. K. Amorphization of the Prototypical Zeolitic Imidazolate Framework ZIF-8 by Ball-Milling. *Chem. Commun.* **48** (63), 7805-7807 (2012). https://doi.org/10.1039/c2cc33773h.

(14) Bennett, T. D., Saines, P. J., Keen, D. A., Tan, J.-C. & Cheetham, A. K. Ball-Milling-Induced Amorphization of Zeolitic Imidazolate Frameworks (ZIFs) for the Irreversible Trapping of Iodine. *Chem. Eur. J.* **19** (22), 7049–7055 (2013). https://doi.org/10.1002/chem.201300216.

(15) Baxter, E. F. et al. Comparison of the Amorphization of Zeolitic Imidazolate Frameworks (ZIFs) and Aluminosilicate Zeolites by Ball-Milling. *Dalton Trans.* **45** (10), 4258–4268 (2016). https://doi.org/10.1039/C5DT03477A.

(16) Bach, S. et al., Hydrate Networks under Mechanical Stress - A Case Study for $Co_3(PO_4)_2 \cdot 8H_2O$. *Eur. J. Inorg. Chem.* **2016** (13–14), 2072–2081 (2016). https://doi.org/10.1002/ejic.201501481.

(17) Schwarz, R. B. & Koch, C. C. Formation of Amorphous Alloys by the Mechanical Alloying of Crystalline Powders of Pure Metals and Powders of Intermetallics. *Appl. Phys. Lett.* **49** (3), 146–148 (1986). https://doi.org/10.1063/1.97206.

(18) Šepelák, V., Bégin-Colin, S. & Le Caër, G. Transformations in Oxides Induced by High-Energy Ball-Milling. *Dalton Trans.* **41** (39), 11927-11948 (2012). https://doi.org/10.1039/c2dt30349c.

(19) Bordet, P. et al. Solid State Amorphization of β-Trehalose: A Structural Investigation Using Synchrotron Powder Diffraction and PDF Analysis. *Cryst. Growth Des.* **16** (8), 4547–4558 (2016). https://doi.org/10.1021/acs.cgd.6b00660.
(20) Mallick, S. et al. Formation of Physically Stable Amorphous Phase of Ibuprofen by Solid State Milling with Kaolin. *Eur. J. Pharm. Biopharm.* **68** (2), 346–351 (2008). https://doi.org/10.1016/j.ejpb.2007.06.003.
(21) Kobayashi, M., Hattori, Y., Sasaki, T. & Otsuka, M. Effect of Ball Milling on the Physicochemical Properties of Atorvastatin Calcium Sesquihydrate: The Dissolution Kinetic Behaviours of Milled Amorphous Solids. *J. Pharm. Pharmacol.* **69** (1), 15–22 (2017)**.** https://doi.org/10.1111/jphp.12636.
(22) Krupa, A. et al. High-Energy Ball Milling as Green Process To Vitrify Tadalafil and Improve Bioavailability. *Mol. Pharm.* **13** (11), 3891–3902 (2016). https://doi.org/10.1021/acs.molpharmaceut.6b00688.
(23) *Ball Milling Towards Green Synthesis: Applications, Projects, Challenges*; Stolle, A., Ranu, B., Eds.; Green Chemistry Series; Royal Society of Chemistry: Cambridge, 2014. https://doi.org/10.1039/9781782621980.
(24) Gilman, J. J. Mechanochemistry. *Science* **274** (5284), 65–65 (1996). https://doi.org/10.1126/science.274.5284.65.
(25) Bellosta von Colbe, J. M., Felderhoff, M., Bogdanović, B., Schüth, F. & Weidenthaler, C. One-Step Direct Synthesis of a Ti-Doped Sodium Alanate Hydrogen Storage Material. *Chem. Commun.* **37**, 4732-4734 (2005). https://doi.org/10.1039/b506502j.
(26) Zevalkink, A. et al. Thermoelectric Properties of Sr3GaSb3 – a Chain-Forming Zintl Compound. *Energy Environ. Sci.* **5** (10), 9121-9128 (2012). https://doi.org/10.1039/c2ee22378c.
(27) Halasz, I. et al. In Situ and Real-Time Monitoring of Mechanochemical Milling Reactions Using Synchrotron X-Ray Diffraction. *Nat. Protoc.* **8** (9), 1718–1729 (2013). https://doi.org/10.1038/nprot.2013.100.
(28) Katsenis, A. D. et al. In Situ X-Ray Diffraction Monitoring of a Mechanochemical Reaction Reveals a Unique Topology Metal-Organic Framework. *Nat. Commun.* **6** (1), 6662 (2015). https://doi.org/10.1038/ncomms7662.
(29) Fischer, F., Wenzel, K.-J., Rademann, K. & Emmerling, F. Quantitative Determination of Activation Energies in Mechanochemical Reactions. *Phys. Chem. Chem. Phys.* **18** (33), 23320–23325 (2016). https://doi.org/10.1039/C6CP04280E.
(30) Ban, V. et al. Innovative *in Situ* Ball Mill for X-Ray Diffraction. *Anal. Chem.* **89** (24), 13176–13181 (2017)**.** https://doi.org/10.1021/acs.analchem.7b02871.
(31) Michalchuk, A. A. L. et al. Ball-Free Mechanochemistry: *In Situ* Real-Time Monitoring of Pharmaceutical Co-Crystal Formation by Resonant Acoustic Mixing. *Chem. Commun.* **54** (32), 4033–4036 (2018)**.** https://doi.org/10.1039/C8CC02187B.
(32) Leukel, S. et al. Trapping Amorphous Intermediates of Carbonates – A Combined Total Scattering and NMR Study. *J. Am. Chem. Soc.* **140** (44), 14638–14646 (2018). https://doi.org/10.1021/jacs.8b06703.
(33) Stawski, T. M. et al. "On Demand" Triggered Crystallization of $CaCO_3$ from Solute Precursor Species Stabilized by the Water-in-Oil Microemulsion. *Phys. Chem. Chem. Phys.* **20** (20), 13825–13835 (2018). https://doi.org/10.1039/C8CP00540K.
(34) Politi, Y. Sea Urchin Spine Calcite Forms via a Transient Amorphous Calcium Carbonate Phase. *Science* **306** (5699), 1161–1164 (2004). https://doi.org/10.1126/science.1102289.
(35) Addadi, L., Raz, S. & Weiner, S. Taking Advantage of Disorder: Amorphous Calcium Carbonate and Its Roles in Biomineralization. *Adv. Mater.* **15** (12), 959–970 (2003). https://doi.org/10.1002/adma.200300381.
(36) Beniash, E., Metzler, R. A., Lam, R. S. K. & Gilbert, P. U. P. A. Transient Amorphous Calcium Phosphate in Forming Enamel. *J. Struct. Biol.* **166** (2), 133–143 (2009). https://doi.org/10.1016/j.jsb.2009.02.001.
(37) Combes, C. & Rey, C. Amorphous Calcium Phosphates: Synthesis, Properties and Uses in Biomaterials. *Acta Biomater.* **6** (9), 3362–3378 (2010). https://doi.org/10.1016/j.actbio.2010.02.017.
(38) Raz, S., Hamilton, P. C., Wilt, F. H., Weiner, S. & Addadi, L. The Transient Phase of Amorphous Calcium Carbonate in Sea Urchin Larval Spicules: The Involvement of Proteins and Magnesium Ions in Its Formation and Stabilization. *Adv. Funct. Mater.* **13** (6), 480–486 (2003). https://doi.org/10.1002/adfm.200304285.
(39) Buljan Meić, I. et al. Comparative Study of Calcium Carbonates and Calcium Phosphates Precipitation in Model Systems Mimicking the Inorganic Environment for Biomineralization. *Cryst. Growth Des.* **17** (3), 1103–1117 (2017). https://doi.org/10.1021/acs.cgd.6b01501.
(40) Gordon, L. M. et al. Amorphous Intergranular Phases Control the Properties of Rodent Tooth Enamel. *Science* **347** (6223), 746–750 (2015). https://doi.org/10.1126/science.1258950.
(41) Belcher, A. M. et al. Control of Crystal Phase Switching and Orientation by Soluble Mollusc-Shell Proteins. *Nature* **381** (6577), 56–58 (1996). https://doi.org/10.1038/381056a0.

(42) Meldrum, F. C. & Cölfen, H. Controlling Mineral Morphologies and Structures in Biological and Synthetic Systems. *Chem. Rev.* **108** (11), 4332–4432 (2008). https://doi.org/10.1021/cr8002856.
(43) Tertuliano, O. A. & Greer, J. R. The Nanocomposite Nature of Bone Drives Its Strength and Damage Resistance. *Nat. Mater.* **15** (11), 1195–1202 (2016). https://doi.org/10.1038/nmat4719.
(44) Wang, Y.-W., Kim, Y.-Y., Stephens, C. J., Meldrum, F. C. & Christenson, H. K. In Situ Study of the Precipitation and Crystallization of Amorphous Calcium Carbonate (ACC). *Cryst. Growth Des.* **12** (3), 1212–1217 (2012). https://doi.org/10.1021/cg201204s.
(45) Gower, L. B. Biomimetic Model Systems for Investigating the Amorphous Precursor Pathway and Its Role in Biomineralization. *Chem. Rev.* **108** (11), 4551–4627 (2008). https://doi.org/10.1021/cr800443h.
(46) Natalio, F. et al. Flexible Minerals: Self-Assembled Calcite Spicules with Extreme Bending Strength. *Science* **339** (6125), 1298–1302 (2013). https://doi.org/10.1126/science.1216260.
(47) Sun, S., Mao, L.-B., Lei, Z., Yu, S.-H. & Cölfen, H. Hydrogels from Amorphous Calcium Carbonate and Polyacrylic Acid: Bio-Inspired Materials for "Mineral Plastics." *Angew. Chem. Int. Ed.* **55** (39), 11765–11769 (2016). https://doi.org/10.1002/anie.201602849.
(48) Koishi, A. et al. Role of Impurities in the Kinetic Persistence of Amorphous Calcium Carbonate: A Nanoscopic Dynamics View. *J. Phys. Chem. C* **122** (29), 16983–16991 (2018). https://doi.org/10.1021/acs.jpcc.8b05189.
(49) Albéric, M. et al. The Crystallization of Amorphous Calcium Carbonate Is Kinetically Governed by Ion Impurities and Water. *Adv. Sci.* **5** (5), 1701000 (2018). https://doi.org/10.1002/advs.201701000.
(50) Kababya, S., Gal, A., Kahil, K., Weiner, S., Addadi, L. & Schmidt, A. Phosphate–Water Interplay Tunes Amorphous Calcium Carbonate Metastability: Spontaneous Phase Separation and Crystallization vs Stabilization Viewed by Solid State NMR. *J. Am. Chem. Soc.* **137** (2), 990–998 (2015). https://doi.org/10.1021/ja511869g.
(51) Cartwright, J. H. E., Checa, A. G., Gale, J. D., Gebauer, D. & Sainz-Díaz, C. I. Calcium Carbonate Polyamorphism and Its Role in Biomineralization: How Many Amorphous Calcium Carbonates Are There? *Angew. Chem. Int. Ed.* **51** (48), 11960–11970 (2012). https://doi.org/10.1002/anie.201203125.
(52) Gebauer, D. et al. Proto-Calcite and Proto-Vaterite in Amorphous Calcium Carbonates. *Angew. Chem. Int. Ed.* **49** (47), 8889–8891 (2010). https://doi.org/10.1002/anie.201003220.
(53) Farhadi-Khouzani, M., Chevrier, D. M., Zhang, P., Hedin, N. & Gebauer, D. Water as the Key to Proto-Aragonite Amorphous $CaCO_3$. *Angew. Chem. Int. Ed.* **55** (28), 8117–8120 (2016). https://doi.org/10.1002/anie.201603176.
(54) Tobler, D. J., Rodriguez Blanco, J. D., Sørensen, H. O., Stipp, S. L. S. & Dideriksen, K. Effect of PH on Amorphous Calcium Carbonate Structure and Transformation. *Cryst. Growth Des.* **16** (8), 4500–4508 (2016). https://doi.org/10.1021/acs.cgd.6b00630.
(55) Jensen, A. C. S., Rodriguez, I., Habraken, W. J. E. M., Fratzl, P. & Bertinetti, L. Mobility of Hydrous Species in Amorphous Calcium/Magnesium Carbonates. *Phys. Chem. Chem. Phys.* **20** (29), 19682–19688 (2018). https://doi.org/10.1039/C8CP01782D.
(56) Lippmann, F. Darstellung und kristallographische Daten von CaCO3xH2O. *Naturwissenschaften* **46** (19), 553–554 (1959). https://doi.org/10.1007/BF00631281.
(57) Dickens, B. & Brown, W. E. Crystal Structure of Calcium Carbonate Hexahydrate at about -120.Deg. *Inorg. Chem.* **9** (3), 480–486 (1970). https://doi.org/10.1021/ic50085a010.
(58) Németh, P. et al. Nanocrystalline Monoclinic $CaCO_3$ Precursor of Metastable Aragonite. *Sci. Adv.* **4** (12), eaau6178 (2018). https://doi.org/10.1126/sciadv.aau6178.
(59) Zou, Z. et al. A Hydrated Crystalline Calcium Carbonate Phase: Calcium Carbonate Hemihydrate. *Science* **363** (6425), 396–400 (2019). https://doi.org/10.1126/science.aav0210.
(60) Ihli, J., Kulak, A. N. & Meldrum, F. C. Freeze-Drying Yields Stable and Pure Amorphous Calcium Carbonate (ACC). *Chem. Commun.* **49** (30), 3134-3136 (2013). https://doi.org/10.1039/c3cc40807h.
(61) Gower, L. B. & Odom, D. J. Deposition of Calcium Carbonate Films by a Polymer-Induced Liquid-Precursor (PILP) Process. *J. Cryst. Growth* **210** (4), 719–734 (2000). https://doi.org/10.1016/S0022-0248(99)00749-6.
(62) Aizenberg, J., Addadi, L., Weiner, S. & Lambert, G. Stabilization of Amorphous Calcium Carbonate by Specialized Macromolecules in Biological and Synthetic Precipitates. *Adv. Mater.* **8** (3), 222–226 (1996). https://doi.org/10.1002/adma.19960080307.
(63) Politi, Y. et al. Role of Magnesium Ion in the Stabilization of Biogenic Amorphous Calcium Carbonate: A Structure−Function Investigation. *Chem. Mater.* **22** (1), 161–166 (2010). https://doi.org/10.1021/cm902674h.
(64) Burns, J. H. & Bredig, M. A. Transformation of Calcite to Aragonite by Grinding. *J. Chem. Phys.* **25** (6), 1281–1281 (1956). https://doi.org/10.1063/1.1743198.
(65) Criado, J. M. & Trillo, J. M. Effects of Mechanical Grinding on the Texture and Structure of Calcium Carbonate. *J. Chem. Soc. Faraday Trans. 1 Phys. Chem. Condens. Phases* **71**, 961-966 (1975). https://doi.org/10.1039/f19757100961.

(66) Northwood, D. O. & Lewis, D. Transformation of Vaterite to Calcite during Grinding. *Am. Mineral.* **53** (11–12), 2089–2092 (1968).
(67) Barriga, C., Morales, J. & Tirado, J. L. Changes in Crystallinity and Thermal Effects in Ground Vaterite. *J. Mater. Sci.* **20** (3), 941–946 (1985). https://doi.org/10.1007/BF00585738.
(68) Leukel, S. et al. Mechanochemical Access to Defect-Stabilized Amorphous Calcium Carbonate. *Chem. Mater.* **30** (17), 6040–6052 (2018). https://doi.org/10.1021/acs.chemmater.8b02339.
(69) Bots, P., Benning, L. G., Rodriguez-Blanco, J.-D., Roncal-Herrero, T. & Shaw, S. Mechanistic Insights into the Crystallization of Amorphous Calcium Carbonate (ACC). *Cryst. Growth Des.* **12** (7), 3806–3814 (2012). https://doi.org/10.1021/cg300676b.
(70) Rodriguez-Blanco, J. D., Shaw, S. & Benning, L. G. The Kinetics and Mechanisms of Amorphous Calcium Carbonate (ACC) Crystallization to Calcite, Viavaterite. *Nanoscale* **3** (1), 265–271 (2011). https://doi.org/10.1039/C0NR00589D.
(71) Wolf, S. E. et al. *Key Eng. Mater.* **672**, 47–59 (2016). https://doi.org/10.4028/www.scientific.net/KEM.672.47.
(72) Rodriguez-Navarro, C., Kudłacz, K., Cizer, Ö. & Ruiz-Agudo, E. Formation of Amorphous Calcium Carbonate and Its Transformation into Mesostructured Calcite. *CrystEngComm* **17** (1), 58–72 (2015). https://doi.org/10.1039/C4CE01562B.
(73) Nebel, H., Neumann, M., Mayer, C. & Epple, M. On the Structure of Amorphous Calcium Carbonate -A Detailed Study by Solid-State NMR Spectroscopy. *Inorg. Chem.* **47** (17), 7874–7879 (2008). https://doi.org/10.1021/ic8007409.
(74) Andersen, F. A. et al. Infrared Spectra of Amorphous and Crystalline Calcium Carbonate. *Acta Chem. Scand.* **45**, 1018–1024 (1991). https://doi.org/10.3891/acta.chem.scand.45-1018.
(75) Parr, R. G. & Pearson, R. G. Absolute Hardness: Companion Parameter to Absolute Electronegativity. *J. Am. Chem. Soc.* **105** (26), 7512–7516 (1983). https://doi.org/10.1021/ja00364a005.
(76) Tortet, L., Gavarri, J. R., Nihoul, G. & Dianoux, A. J. Study of Protonic Mobility in CaHPO4·2H2O (Brushite) and CaHPO4(Monetite) by Infrared Spectroscopy and Neutron Scattering. *J. Solid State Chem.* **132** (1), 6–16 (1997). https://doi.org/10.1006/jssc.1997.7383.
(77) Brangule, A. & Gross, K. A. Importance of FTIR Spectra Deconvolution for the Analysis of Amorphous Calcium Phosphates. *IOP Conf. Ser. Mater. Sci. Eng.* **77**, 012027 (2015). https://doi.org/10.1088/1757-899X/77/1/012027.
(78) Plyler, E. K. & Acquista, N. Infrared Absorption Spectra of Cyclo-Hydrocarbons. *J. Res. Natl. Bur. Stand.* **43** (1), 37-48 (1949). https://nvlpubs.nist.gov/nistpubs/jres/43/jresv43n1p37_A1b.pdf.
(79) Hing, A. W., Vega, S. & Schaefer, J. Transferred-Echo Double-Resonance NMR. *J. Magn. Reson.* **96** (1), 205–209 (1992). https://doi.org/10.1016/0022-2364(92)90305-Q
(80) Rothwell, W. P., Waugh, J. S. & Yesinowski, J. P. High-Resolution Variable-Temperature Phosphorus-31 NMR of Solid Calcium Phosphates. *J. Am. Chem. Soc.* **102** (8), 2637–2643 (1980). https://doi.org/10.1021/ja00528a020.
(81) Catti, M., Ferraris, G. & Filhol, A. Hydrogen Bonding in the Crystalline State. CaHPO4 (Monetite), P1 or P1? A Novel Neutron Diffraction Study. *Acta Crystallogr. B* **33** (4), 1223–1229 (1977). https://doi.org/10.1107/S0567740877005706.
(82) Gras, P. et al. From Crystalline to Amorphous Calcium Pyrophosphates: A Solid State Nuclear Magnetic Resonance Perspective. *Acta Biomater.* **31**, 348–357 (2016). https://doi.org/10.1016/j.actbio.2015.10.016.
(83) Giordani, M. & Beruto, D. Effect of Vaporization Rate on Calcium Carbonate Nucleation from Calcium Hydrogen Carbonate Aqueous Solutions. *J. Cryst. Growth* **84** (4), 679–682 (1987). https://doi.org/10.1016/0022-0248(87)90060-1.
(84) Beruto, D. & Giordani, M. Calcite and Aragonite Formation from Aqueous Calcium Hydrogencarbonate Solutions: Effect of Induced Electromagnetic Field on the Activity of CaCO3 Nuclei Precursors. *J. Chem. Soc. Faraday Trans.* **89** (14), 2457-2461 (1993). https://doi.org/10.1039/ft9938902457.
(85) *A Dictionary of Chemistry*, 6th ed.; Daintith, J., Ed.; Oxford paperback reference; Oxford University Press: New York, 2008.
(86) Shannon, R. D. Revised Effective Ionic Radii and Systematic Studies of Interatomic Distances in Halides and Chalcogenides. *Acta Crystallogr. Sect. A* **32** (5), 751–767 (1976). https://doi.org/10.1107/S0567739476001551.
(87) Xu, B., Hirsch, A., Kronik, L. & Poduska, K. M. Vibrational Properties of Isotopically Enriched Materials: The Case of Calcite. *RSC Adv.* **8** (59), 33985–33992 (2018). https://doi.org/10.1039/C8RA06608F.
(88) Rudolph, W. W., Fischer, D. & Irmer, G. Vibrational Spectroscopic Studies and Density Functional Theory Calculations of Speciation in the CO_2 —Water System. *Appl. Spectrosc.* **60** (2), 130–144 (2006). https://doi.org/10.1366/000370206776023421.
(89) Garand, E. et al. Infrared Spectroscopy of Hydrated Bicarbonate Anion Clusters: $HCO_3^-(H_2O)_{1-10}$. *J. Am. Chem. Soc.* **132** (2), 849–856 (2010). https://doi.org/10.1021/ja9093132.

(90) Eckert, H. Dipolar 31P NMR Spectroscopy of Crystalline Inorganic Phosphorus Compounds. *Solid State Nucl. Mugnetic Reson.* **1**, 73–83 (1992).
(91) Gee, B. & Eckert, H. Cation Distribution in Mixed-Alkali Silicate Glasses. NMR Studies by $^{23}Na-\{^{7}Li\}$ and $^{23}Na-\{^{6}Li\}$ Spin Echo Double Resonance. *J. Phys. Chem.* **100** (9), 3705–3712 (1996). https://doi.org/10.1021/jp9521722.
(92) Eckert, H. Short and Medium Range Order in Ion-Conducting Glasses Studied by Modern Solid State NMR Techniques. *Z. Für Phys. Chem.* **224** (10–12), 1591–1654 (2010). https://doi.org/10.1524/zpch.2010.0030.
(93) Van Vleck, J. H. The Dipolar Broadening of Magnetic Resonance Lines in Crystals. *Phys. Rev.* **74** (9), 1168–1183 (1948). https://doi.org/10.1103/PhysRev.74.1168.
(94) Jansen, M., Schön, J. C. & van Wüllen, L. The Route to the Structure Determination of Amorphous Solids: A Case Study of the Ceramic Si3B3N7. *Angew. Chem. Int. Ed.* **45 45** (26), 4244–4263 (2006). https://doi.org/10.1002/anie.200504193.
(95) Hoeher, A., Mergelsberg, S., Borkiewicz, O. J., Dove, P. M. & Michel, F. M. A New Method for *in Situ* Structural Investigations of Nano-Sized Amorphous and Crystalline Materials Using Mixed-Flow Reactors. *Acta Crystallogr. Sect. Found. Adv.* **75** (5), 758–765 (2019). https://doi.org/10.1107/S2053273319008623.
(96) Ferrero, E. E., Martens, K. & Barrat, J.-L. Relaxation in Yield Stress Systems through Elastically Interacting Activated Events. *Phys. Rev. Lett.* **113** (24), 248301 (2014). https://doi.org/10.1103/PhysRevLett.113.248301.
(97) Pritzker, K. P. H. Calcium Pyrophosphate Crystal Formation and Dissolution. In *Calcium Phosphates in Biological and Industrial Systems*; Amjad, Z., Ed.; Springer US: Boston, MA, 1998; pp. 277–301. https://doi.org/10.1007/978-1-4615-5517-9_12.
(98) Hahn, E. L. Spin Echoes. *Phys. Rev.* 80 (4), 580–594 (1950). https://doi.org/10.1103/PhysRev.80.580.
(99) Makowka, C. D., Slichter, C. P. & Sinfelt, J. H. Probe of the Surface of a Heterogeneous Catalyst: Double NMR of Carbon Monoxide Chemisorbed on Highly Dispersed Platinum. *Phys. Rev. Lett.* **49** (6), 379–382 (1982). https://doi.org/10.1103/PhysRevLett.49.379.
(100) Dippel, A.-C. et al. Beamline P02.1 at PETRA III for High-Resolution and High-Energy Powder Diffraction. *J. Synchrotron Radiat.* **22** (3), 675–687 (2015). https://doi.org/10.1107/S1600577515002222.
(101) Filik, J. et al. Processing Two-Dimensional X-Ray Diffraction and Small-Angle Scattering Data in *DAWN 2*. *J. Appl. Crystallogr.* **50** (3), 959–966 (2017). https://doi.org/10.1107/S1600576717004708.
(102) Soper, A. K. & Barney, E. R. Extracting the Pair Distribution Function from White-Beam X-Ray Total Scattering Data. *J. Appl. Crystallogr.* **44** (4), 714–726 (2011). https://doi.org/10.1107/S0021889811021455.